



Yttrium complexation and hydration in chloride-rich hydrothermal fluids: A combined ab initio molecular dynamics and in situ X-ray absorption spectroscopy study

Qiushi Guan, Yuan Mei, Barbara Etschmann, Denis Testemale, Marion Louvel, Joël Brugger

► To cite this version:

Qiushi Guan, Yuan Mei, Barbara Etschmann, Denis Testemale, Marion Louvel, et al.. Yttrium complexation and hydration in chloride-rich hydrothermal fluids: A combined ab initio molecular dynamics and in situ X-ray absorption spectroscopy study. *Geochimica et Cosmochimica Acta*, 2020, 281, pp.168-189. 10.1016/j.gca.2020.04.015 . hal-03012822

HAL Id: hal-03012822

<https://hal.science/hal-03012822>

Submitted on 11 Dec 2020

HAL is a multi-disciplinary open access archive for the deposit and dissemination of scientific research documents, whether they are published or not. The documents may come from teaching and research institutions in France or abroad, or from public or private research centers.

L'archive ouverte pluridisciplinaire **HAL**, est destinée au dépôt et à la diffusion de documents scientifiques de niveau recherche, publiés ou non, émanant des établissements d'enseignement et de recherche français ou étrangers, des laboratoires publics ou privés.

**Yttrium complexation and hydration in chloride-rich hydrothermal
fluids: a combined *ab initio* molecular dynamics and *in situ* X-ray
absorption spectroscopy study**

Qiushi Guan^{1,2}, Yuan Mei^{2*}, Barbara Etschmann¹, Denis Testemale³, Marion Louvel⁴,
Joël Brugger^{1*}

1. School of Earth, Atmosphere and the Environment, Monash University,
Clayton, VIC 3800, Australia

2. CSIRO Mineral Resources, Kensington WA 6152, Australia

3. CNRS, Université Grenoble Alpes, Institut NEEL, F-38000 Grenoble, France

4. Institute for Mineralogy, WWU Muenster, D-48149 Germany

*Corresponding author: Yuan Mei (Yuan.Mei@csiro.au); Joël Brugger
(joel.brugger@monash.edu)

Abstract

Accurate knowledge of rare earth elements (REE) speciation in high pressure –
high temperature fluids is required to model REE transport and precipitation in
subduction zones and magmatic-hydrothermal environments, and the formation of
rare metal deposits. Recent experiments (lanthanum, ytterbium, erbium) have
demonstrated that REE chloride complexes are the main REE form in many
hydrothermal fluids (Migdisov, et al., 2016). However, the speciation of yttrium

(Y(III)), a cation with an ionic radius similar to that of Ho(III), remains poorly constrained in chloride-rich hydrothermal solutions.

We used *ab initio* molecular dynamics (MD) simulations to calculate the nature of Y(III)-Cl complexes and the thermodynamic properties of these species at temperatures up to 500 °C and pressures of 800 bar and 1000 bar. The MD results were complemented by *in-situ* X-ray absorption spectroscopy (XAS) measurements. Our results indicate that at temperature below 200 °C, chloro-complexes do not form readily, even in highly concentrated brines. At ambient condition, the Y(III) aqua ion binds to eight water molecules in a square antiprism geometry, which is consistent with previous *ab initio* studies (Ikeda, et al., 2005). The thermodynamic integration method was employed to calculate the formation constants ($\log\beta$) of Y(III)-Cl⁻ complexes in two simulation boxes containing different Y:Cl ratios; we obtained very consistent results of the standard $\log\beta$ of same complexes from the two independent calculations, which confirms that the thermodynamic integration method is reliable and not significantly affected by technical limitations in box size, box composition, or simulation times.

Based on the derived formation constants, we fit Modified Ryzhenko–Bryzgalin (MRB) equation of state parameters, which enable extrapolation of the formation constants at elevated temperature and pressure. The results are consistent with the XAS data, and show that the stability of Y(III)-Cl complexes increases with increasing temperature, Y(III) forming high order Cl⁻ complexes (up to YCl₄⁻) in high

43 salinity solutions at high temperature and $\text{pH} = 3$. We also compare the extrapolated
44 $\log\beta$ with the available data for other REE at 150 °C, 200 °C and 250 °C. At 200 °C,
45 yttrium behaves more like a heavy REE, but from 200 °C to 250 °C, the $\log\beta$ of
46 Y(III)-Cl complexes increases dramatically and behave more like the light REE. The
47 difference of Cl^- dominant species between Ho(III) (HoCl^{2+}) and Y(III) (YCl_2^+) may
48 account for the formation of anomalous Y/Ho ratios in some hydrothermal
49 environments.

50

51 Keywords: Yttrium; *ab initio* molecular dynamics; XAS; yttrium chloride aqueous
52 speciation; thermodynamics; rare earth elements.

53

54

55

1. Introduction

Demand for rare earth elements (REE: La to Lu) plus Y has increased in the past decades due to their use in fast-growing industrial applications (e.g., energy, mobility and special alloys; Krishnamurthy, 2016). Combined with strategic issues related to current concentration of REE production within China, this has led to world-wide efforts to secure new geological sources of REE (Weng et al., 2015; Ram et al. 2018). The world's largest REE deposit formed by a combination of magmatic and hydrothermal processes (Bayan Obo, China; Ling et al., 2013). REE are mobile in many hydrothermal systems (e.g., Iron Oxide Copper Gold deposits and their alteration halos; (Kontonikas-Charos et al., 2018; Xing et al., 2019), and since REE behave coherently through geochemical processes, they can be used as tracers for fluid-rock interaction (e.g., Bau and Dulski, 1995; Brugger et al., 2008). Over the past decade, a number of experimental studies have dramatically improved our understanding of REE speciation in natural water at elevated temperature, e.g. *in situ* measurements at high temperature-pressure for Yb (Louvel et al. 2015) and Eu (Liu et al. 2017); solubility experiments of REE+Y-fluoride (Loges et al. 2013; Migdisov 2009); *in situ* spectrophotometric studies of REE chloride and sulfate complexes (Migdisov and Williams-Jones, 2008; Migdisov et al. 2008). As reviewed by Migdisov et al. (2016), the nature of REE complexes (e.g., chloride versus fluoride or hydroxide complexes) affects mineral solubility, and is controlled by temperature, pressure and solution composition.

A molecular-level understanding of the coordination geometry and hydration of the complexes is key to reliable extrapolations of thermodynamic properties that can be also used to model metal mobility beyond the conditions covered by experiments (Brugger et al., 2016). Chloride is the most common ligand in many geo-fluids, and despite the fact that REE fluoride complexes are much stronger than chloride complexes (Haas et al., 1995; Wood, 1990), chloride complexes are considered as the main transporting ligands in many hydrothermal fluids, especially at high temperature, since the stability of chloride complexes increases with increasing temperature relative to fluoride complexes, and the activity of the fluoride ion is limited by the strong association of hydrofluoric acid at elevated temperature and the low solubility of fluorine-containing phases such as fluorite, apatite, and biotite (Gammons et al., 1996; Migdisov et al., 2009; Xing et al. 2019).

The similar chemical properties of REE *sensu stricto* (lanthanides) are a result of their valence electrons in $4f$ -orbitals; these f -electrons are buried deep within the atom and shielded by $4d$ and $5p$ electrons and do not take part in bonding. Yttrium is often grouped with REE because its ionic radius (0.900 \AA for Y^{3+}) is close to that of the heavy REE (Ho^{3+} at 0.901 \AA ; Shannon, 1976). However, due to its lack of f -electrons ($[\text{Kr}] 4d^1 5s^2$), Y(III) shows significant differences in behavior compared to REE *sensu stricto*. For example, Loges (2013) showed that at temperatures below 250°C , the dominant Y(III) fluoride complex is YF_2^{2+} , compared to REEF_2^+ (HoF_2^+). These differences can result in contrasting mobility of Y and REE in hydrothermal systems

98 (Williams-Jones, 2009), leading to the concept of ‘yttrium anomaly’ (Bau and Dulski,
99 1995).

100 Several experiments have been conducted on the hydration of Y(III) at low
101 temperature (Table 1). At room temperature, the Y(III) aqua ion is generally
102 recognized to have a coordination of 8 and a square antiprism structure (references in
103 Table 1). The early *in-situ* XAS study of Ragnarsdottir et al. (1998) provides the only
104 experimental data on Y(III) hydration under hydrothermal conditions. Ragnarsdottir et
105 al. (1998) obtained a higher than expected Y(III) hydration number at room
106 temperature (9.1 – 10.3), and showed a small decrease in hydration number to 8 at
107 temperature of 250 °C, with no further dehydration observed upon heating to 340 °C.

108 There are only a few studies about Y(III) chloride complexing, and again
109 Ragnarsdottir et al. (1998) is the only experimental study extending to hydrothermal
110 conditions (Table 1). Conclusions regarding the extent of Y-Cl complexation differ.
111 On one hand, Allen et al. (2000)’s EXAFS study found no evidence for Cl⁻ bonded
112 with Y(III) at ambient temperature, even in brines containing up to 14 m Cl⁻.
113 Ragnarsdottir et al. (1998) similarly found no evidence of Y-Cl complexing in a 0.1 m
114 YCl₃ solution to 340 °C, and in a 0.1 m YCl₃ + 0.23 m HCl + 2 m NaCl solution to
115 250 °C (Cl_{tot} = 2.53 m). On the other hand, Luo and Byrne (2001) report a stability
116 constant of 0.65 ± 0.05 for the formation of YCl²⁺ (reaction $Y^{3+} + Cl^- = YCl^{2+}$) at
117 25 °C and zero ionic strength, and concluded that Y³⁺ formed weak complexes with
118 Cl⁻. Combining neutron scattering and EXAFS spectroscopy, Bowron and

Diaz-Moreno (2007) also support the formation of Y-Cl complexes in 1 m YCl₃ solution at room temperature, with a hydration number of 7.4 ± 0.5 in the distance between 2.1 Å and 3.3 Å, and 0.8 ± 0.2 Cl⁻ between 2.5 Å and 3.5 Å, from the radial distribution functions of Y-O and Y-Cl. Rudolph and Irmer (2015) concluded in a recent Raman study that Y(III) and Cl⁻ can form weak chloro-complexes at room temperature in YCl₃+HCl solutions (2.03 M YCl₃ in 1.0 M and 4 M HCl). They propose that Y exists in 8-fold coordination as [Y(H₂O)_{8-n}Cl_n]⁺³⁻ⁿ in these solutions, with chloride numbers $n \leq 2$. Stefanski and Jahn (2019) studied Y(III) speciation in chloride- and fluoride-rich brines under subduction conditions (800 °C, 13/45 kbar) with *ab initio* molecular dynamics, and concluded that chloride complexes [Y(H₂O)₂₋₇Cl₁₋₅]^{+3-n(Cl)} are important species of Y mass transfer in subduction zones.

Table 1. Structure of aqueous Y(III) in literature

In this study, we combined *ab initio* molecular dynamics (MD) simulations and *in situ* XAS measurements to quantify the nature, geometry, and stability of Y(III) complexes in chlorine-rich fluids from room temperature to 500 °C, 1000 bar. In particular, the formation constants of Y(III)-Cl complexes were calculated from *ab initio* MD using the thermodynamic integration method. Our previous studies have demonstrated that the combination of *ab initio* computational chemistry and *in situ* spectroscopic experiments is a powerful approach to determining element speciation and geometry in hydrothermal fluids (Mei et al., 2015a,b, 2016; Brugger et al., 2016; Etschmann et al., 2018, 2019), providing accurate speciation data that can be used to

provide extrapolations to conditions beyond experimental scope.

2. Method

2.1 *Ab initio* molecular dynamics

The *ab initio* MD simulations were conducted with Car-Parrinello Molecular Dynamics (CPMD, version 3.1.17, Car and Parrinello, 1985). In CPMD, the electrons were treated as plane wave basis sets using density functional theory. The interactions between valence electrons were depicted by BLYP exchange correlation functional (Becke, 1988; Lee et al., 1988), which produces a good description of the structural properties of water including O–O interaction, angular distributions, coordination numbers, H-bond statistics, and radial distribution functions when compared with experiments (Gillan et al., 2016; Lin et al., 2012). However, most generalized gradient approximation functionals, including BLYP, tend to overestimate the ordering of the structure of liquid water at ambient condition (e.g., Sprik, et al. 1996, Mei et al., 2018). Bankura et al. (2014) showed that BLYP best reproduces the properties of water at ambient conditions when using an elevated temperature for the simulations, and it could be argued that there is a temperature offset of approximately 55°C between the computed data and experiment in terms of solvent properties. Despite these limitations, many previous studies obtained accurate results of aqueous metal-ligand complexations at both room and high temperature using the BLYP functional (e.g. Mei et al., 2015b; Stefanski and Jahn, 2019). A timestep of 3 a.u. (0.073 fs) and fictitious mass of 400 a.u. to all atoms were employed in the simulation.

We used the NVT ensemble to conduct the simulations. The density of the solution was chosen according to the equation of state of NaCl solution at similar chloride concentration at targeted T and P (Driesner, 2007; Driesner and Heinrich, 2007). The temperature was fixed with Nosé-Hoover chain thermostat for ions and electrons. Periodic boundary condition was applied to eliminate surface effects.

In total, 15 *ab initio* MD simulations were conducted over a range of temperatures (25-500 °C), pressures (1, 800 and 1000 bar), and compositions (simulation boxes containing 1 yttrium(III) ion, 3 to 5 chloride ion, and 55 or 110 H₂O molecules) relevant for a wide range of hydrothermal systems; the simulation details are listed in Table 2. All the MD simulations were conducted for 16-30 picoseconds (ps) in order to achieve good statistics. As discussed in our previous study (Mei et al., 2013a), the size of the simulation boxes and times in this study can provide solid results within manageable computation resources. The time-averaged stoichiometric and geometric information was obtained with VMD (Humphrey et al., 1996). The coordination numbers were retrieved from radial distribution functions (RDF), and their errors were estimated from the change of RDF integral at the distance range of 2.75 Å - 3.25 Å for Y-O, and 2.9 Å – 3.2 Å for Y-Cl. The Debye-Waller factor were calculated following equations in section 2.3 in Campbell et al. (1999).

Table 2. simulation details of *ab initio* MD

2.2 *Ab initio* thermodynamic integration

The *ab initio* MD results reveal the structure of Y(III)-Cl complexes at different P-T. However, *ab initio* MD is very resource-intensive: for example, obtaining 1 picosecond of real time data requires ~6,800 CPU hours for a simulation box containing 111 waters with density of 0.73 g/cm³ at 450 °C, and ~1,300 CPU hours for a simulation box containing 55 waters with density of 0.90 g/cm³ at 350 °C. This limits the timescale of MD simulations to 10's of picoseconds (ps). Under these conditions, observation of the distribution of species (i.e., statistical appraisal of association/dissociation reactions of ligands) in a solution can be beyond current computational capabilities, since ligand exchange rates are in the timescale of nanoseconds or microseconds for many aqua- and chloride complexes. For example, the water residence time of Ho³⁺ is 4.67 ns at 298 K (Cossy et al., 1989), with Y³⁺ expected to have a value within the same order of magnitude based on similarities in the ionic radius of Y(III) and Ho(III) (Shannon, 1979). The residence times of the Cl⁻ ligand in complexes of the transition metals Au(III), Zn(II) and Cd(II) are around 9.3 ms, 251 μs and <32 μs, respectively (Sharps et al., 1993). Even though ligand residence times decrease with temperature to a point where individual ligand exchange reactions can be easily observed via *ab initio* MD, the exchange rates are generally not sufficient to allow measurements of the relative complexes stabilities from the distribution of species in the simulations. Instead, the thermodynamic integration method (Sprik, 1998; Sprik & Ciccotti, 1998) was used to obtain

quantitative thermodynamic information on ligand exchange reactions. In this method, the limits imposed by the slow exchange kinetics in most ligand exchange reactions are lifted by measuring the free energy difference in the ligand exchange reaction along a user-defined reaction path, taking advantage of the fact that this energy difference is independent of the chosen reaction path. The method implementation is similar to that used by Mei et al. (2013a), and only a short summary is provided here; specific details of employing thermodynamic integration to calculate formation constant of Y(III) chloride complexes are described in section 3.4. We chose to investigate the chloride dissociation reactions, i.e.



The reaction paths were defined by constraining the Y(III)-Cl distances (r) step-wise along coordinates that vary from the equilibrium bond (distance r_I) to a distance where the Cl^- ion does not interact with the complex (bulk distance, r_{II}). The mean constraint force ($f(r)$) required to maintain the Y(III)-Cl distance at r was obtained at each step. At each distance r , the simulation was conducted for at least 6 ps to sample a significant ensemble of possible configurations of Y(III)-Cl complexes and the surrounding solvent. The Helmholtz free energy of the ligand exchange reaction ($\Delta A_{I \rightarrow II}$) was retrieved by integrating $f(r)$ over the constrained distance (r_I to r_{II}) (Sprik et al., 1998; Sprik & Michiel, 2000):

$$\Delta A_{I \rightarrow II} = - \int_{r_I}^{r_{II}} f(r) dr \quad (2)$$

The Helmholtz and Gibbs free energies are related by

$$\Delta_r G = \Delta A_{I \rightarrow II} + V \int_{P_0}^P dP \quad (3)$$

where V is the volume of the box and $\int_{P_0}^P dP$ is the energy contribution due to the pressure change associated with the ligand exchange at constant volume. As shown in our previous work (Mei et al. 2013a), the contribution of $\int_{P_0}^P dP$ is small and thus is neglected. The standard Gibbs free energies of reactions ($\Delta_r G^\ominus$) were calculated from the Gibbs free energy of reactions ($\Delta_r G$) using

$$\Delta_r G^\ominus = \Delta_r G + RT \ln \frac{c_A \gamma_A \cdot c_B \gamma_B}{c_C \gamma_C \cdot c_D \gamma_D} \quad (4)$$

where c_i are the concentration of the compounds of reaction $A + B \rightarrow C + D$, and γ_i are the activity coefficients of each species. By assuming $\gamma_i = 1$ the Gibbs free energy of reactions of ideal solution ($\Delta_r G^{\ominus, c}$) were obtained. However, in this work, all simulations were conducted with high relatively concentrations (i.e. 3 m Cl^- and 5 m Cl^-) and high ionic strengths. The activity coefficients of the ions involved in the ligand exchange reactions were estimated with the B-dot extension of Debye-Hückel theory (Helgeson, 1981):

$$\log \gamma_i = -\frac{z_i^2 A_\gamma I^{1/2}}{1 + a_i B_\gamma I^{1/2}} + \dot{B}_\gamma I \quad (5)$$

where z_i is the charge of ion i ; I is the ionic strength in molality; a_i is the ion size parameter (\AA); A_γ and B_γ are defined in Tables 1 and 2 in Helgeson and Kirkham (1974), \dot{B}_γ is an empirical parameter taken from Oelkers and Helgeson (1990). Finally, the formation constants (K^\ominus) for the ligand exchange reactions were calculated from

$$\Delta_r G^\ominus = -RT \ln K^\ominus \quad (6)$$

where R is the gas constant and T is temperature in Kelvin.

The uncertainties of the Gibbs free energies and $\log K^\ominus$ values in *ab initio* thermodynamic integrations were estimated with the method proposed by Allen and Tildesley (1987). This method has been used by Rodinger et al. (2005) and Mei et al. (2018) to estimate the uncertainty of thermodynamic integration. The statistical error of each mean constraint force ($\Delta f(r)$) was calculated as the standard deviation of the mean force divided by a statistical inefficiency coefficient; this error includes both the systematic and statistical errors (detail in section 6.4 in Allen and Tildesley, 1987). The statistical error of $\Delta_r G$ and $\log K^\ominus$ are obtained by accumulating $\Delta f(r)$ over distance ($-\int_{r_I}^{r_{II}} \Delta f(r) dr$). The error of cumulative formation constant was measured using standard propagation rules.

2.3 Thermodynamic properties

To obtain the formation constants of Y(III)-Cl complexes over a broad temperature and pressure range, we fitted the MD calculation results with the modified Ryzhenko–Bryzgalin (MRB) model (Ryzhenko et al., 1985):

$$\log K_{(T,P)} = -\frac{T_r}{T} \log K_{(T_r,P_r)} + B_{(T,P)} \left(A_{(zz/a)} + \frac{B_{(zz/a)}}{T} \right) \quad (7)$$

where K is the formation constant of Y(III)-Cl⁻ complexes at certain T and P ; T_r , P_r are the reference temperature and pressure (*i.e.*, 25 °C and 1 bar), and $A_{(zz/a)}$ and $B_{(zz/a)}$ are fitted empirical parameters (Shvarov and Bastrakov, 1999). The $B_{(T,P)}$ parameter is a species-independent function computed from the dissociation constant of water from Marshall and Franck (1981) (equation (2)). The fitting was done using the

OptimC code developed by Shvarov (2008, 2015). The modeling of speciation was conducted using the Matlab code BeerOz (Brugger, 2007).

2.4 XAS measurements and data processing

Experimental solutions for XAS measurements were prepared by dissolving the appropriate amounts of solids in acidified water. The compositions of the solutions are listed in Table 3. Analytical grade yttrium chloride ($\text{YCl}_3 \cdot 6\text{H}_2\text{O}$), LiCl, NaCl, 37% HCl and MilliQ water were used to prepare the solutions.

Table 3. XAS solution

The speciation of yttrium in Cl-rich fluids was characterised via *in-situ* X-ray absorption measurements (XAS) using the high temperature-high pressure cell developed at the Institut Neel/ESRF (Bruyère et al., 2008; Testemale et al., 2005). This cell consists of an external water-cooled pressure vessel equipped with three beryllium windows enabling collection of simultaneous fluorescence and transmission signals. The sample is contained inside a glassy carbon tube with an internal diameter of 4 mm that is placed inside a small cylindrical resistive heater. Pressure is applied to the sample by two glassy carbon pistons, using helium as a pressure medium, while temperature is recorded by two thermocouples placed within the heating element. Although the thermocouple sits near the sample, it is placed outside the sample and the temperature of the fluid at the beam location needs to be calibrated (e.g., Brugger et al., 2007; Etschmann et al., 2010; Liu et al., 2011; Louvel et al., 2017). To do so,

the density of pure water is calculated from measurements of the absorbance and X-ray mass attenuation coefficients tabulated by Chantler (1995), and then compared to that from the equation of state of pure water (NIST database, Lemmon et al., 2000). This method provides a direct measurement of the temperature at the beam position; temperature accuracy is better than 5 °C, and temperature varied within less than 1 °C during the measurements. Pressure was read from a calibrated Bourdin gauge with a precision better than 5 bars; during the experiment, pressure was maintained with 1 bar by the PID system (Bruyère et al., 2008).

Yttrium K-edge (17,038 eV) X-ray Absorption Near Edge Structure (XANES) and Extended X-ray Absorption Fine Structure (EXAFS) spectra were collected up to 500 °C at 800 bars at the FAME beamline at the European Synchrotron Research Facility (ESRF) in Grenoble, France. The ESRF is a 6.03 GeV ring, and operating in 7/8 multi-bunch mode it has a maximum current of 200 mA. FAME is a bending magnet beamline (see Proux et al., 2005 for details), and its double crystal Si(220) monochromator provides an energy resolution of 0.87 eV at the Y K edge energy. A focused beam size of FWHM 220 x 145 μm^2 was used. The incident and transmitted beam intensities I_0 and I_1 were measured with Si diodes, and a Canberra 30 element solid state fluorescence detector was used for detecting fluorescence data. The beam energy was calibrated with an Y foil, such that the maximum of the first derivative was at 17,038 eV.

XANES and EXAFS data were analysed with the HORAE package (Ravel and

Newville, 2005), using FEFF version 9 (Rehr et al., 2009); E_0 was defined as the maximum of the first derivative. Reported errors in EXAFS parameters ($1-\sigma$) are those calculated by the Artemis program (part of HORAE).

2.5 *ab initio* XANES simulation

Ab initio XANES simulations were conducted using the FDMNES program (Joly, 2001; Joly et al., 2009) following the method described in previous studies of metal complexing (Testemale et al., 2009; Tian et al., 2014; Etschmann et al., 2018). The photo absorption cross sections were calculated using the Finite Difference Method (FDM), which allows accurate calculations especially in the case of low-symmetry structures compared to methods based on the Muffin-Tin approximation, but at a cost of increased computing resources (Joly, 2001; Brugger, et al., 2007). To compare with the experimental spectra, the calculations were convoluted with a Lorentzian function of energy-dependent width to reproduce the core-hole lifetime broadening (3.52 eV; Krause and Oliver, 1979) and the inelastic plasmon interactions with the photoelectron. A Gaussian function (width of 0.87 eV) was employed to account for the energy resolution of the beamline at the convolution. In this study, theoretical spectra were calculated for: 1) crystalline Y_2O_3 solid (Santos et al., 2005), as a reference to estimate the accuracy of the simulations; 2) regular predefined square antiprism structures YO_8 ; 3) regular triangular antiprism structures and selected representative Y-O-Cl complexes (with total coordination of 6) from MD calculation at each condition (Figure 1a,c,d,e); 4) average of at least 50 MD whole

boxes at each condition. The radius cutoffs of all calculations were 5 Å.

3. Results

3.1 Geometrical properties from *ab initio* MD

Unconstrained MD simulations were performed in four solutions with different concentrations of Cl⁻ (Table 2) at 25 °C, 200 °C, 350 °C, 450 °C and 500 °C. The simulation results are summarized in Table 4. The snapshots of different Y(III)-Cl⁻ complexes and pair distribution functions of Y-O and Y-Cl of each solutions are shown in Figure 1 and 2.

Table 4. simulation results from *ab initio* MD

Figure 1. snapshots of Y(III)-Cl

Figure 2. RDF

In box 1 (Y:Cl = 1:3), at ambient conditions (25 °C, 1 bar), two jobs were conducted to test the stability of Y(III)-Cl complexes. In job 1a(1), the simulation started with [Y(OH₂)₈]³⁺, and this configuration remained stable during the whole simulation. In job 1a(2), the initial configuration was [Y(OH₂)₇Cl]²⁺ and Cl⁻ dissociated from Y(III) in less than 1 ps (Fig. 3a), and [Y(OH₂)₈]³⁺ remained stable for the rest of the simulation. The eight water molecules in the first shell of Y³⁺ formed an antiprism structure (Fig. 1a, 1b), which is consistent with previous MD and XANES studies (Table 1). The Y-O bond distance (2.42 Å) from MD is also within the range of values from literature (2.36 Å to 2.51 Å, reference in Table 1), and close to our XAS results (2.37 to 2.39 Å, section 3.2). No evidence of Cl⁻

bonding with Y(III) was found for this Cl concentration. The oscillations of Y-O bond distance indicate Debye-Waller factors of 0.0106 \AA^2 and 0.0107 \AA^2 for job 1a(1) and 1a(2), respectively.

Simulation 1b was run at 200 °C and 800 bar for a total of 30.17 ps, starting with the $[\text{Y}(\text{OH}_2)_6\text{Cl}_2]^+$ complex as the initial configuration. The calculated hydration number is 5.2. One Cl^- dissociated from Y(III) from 14.6 ps to 22.6 ps (Fig. 3b), which leads to an average chloride coordination number of 1.8 over the simulation time. The RDFs in Fig. 2 indicate Y-Cl and Y-O bond distances of 2.65 Å and 2.36 Å, respectively. At 350 °C, 800 bar (simulation 1c), the total coordination number of Y(III) further decrease to 6.5. Two water molecules bonded with Y(III) in the initial configuration detached from Y(III) within the first picosecond. The two Cl^- remained bonded to Y(III) at an average distance of 2.62 Å over the 23.87 ps simulation, *i.e.* no ligand change was observed. At 500 °C, 800 bar and 1000 bar (simulation 1d and 1e), the final species was $[\text{Y}(\text{OH}_2)_5\text{Cl}_3]^0$. The Y-Cl and Y-O bond lengths (Fig. 2) were 2.55 – 2.56 Å and 2.44 Å, respectively.

Figure 3. Y-Cl distance over time

Simulations of box 2, 3, 4 were conducted with different Cl^- concentrations ($\text{Y}:\text{Cl} = 1:4, 1:5, 1:2.5$), and run at the same P-T conditions as box 1 except room temperature. The bond distances and total coordination numbers calculated within each box are consistent at each P-T condition (Table 2). At 200 °C, the coordination of Cl^- in box 4a is 1, whereas it is ~2 in the other boxes, suggesting an effect of

increasing Cl contents on the stability of Y-Cl complexes. At 500 °C, 1000 bar, coordination of Cl⁻ is 2 for simulation 2c. In simulation 4c (Cl⁻ concentration of 5 m), at 450 °C, 800 bar, the initial complex [Y(OH₂)₅Cl₃]⁰ lost two waters within the first 1.5 ps, and became [Y(OH₂)₃Cl₃]⁰, which remained stable for the last 15.41 ps. Interestingly, the coordination number of Cl⁻ reaches 4 in simulation 3c (Y:Cl = 1:5; 500 °C, 1000 bar), with the average number of water molecules down to 1.7.

In general, the total coordination number decreases from 8 to 6 and Y(III)-Cl⁻ complexes become more stable as temperature increases from 25 °C to 500 °C. At high temperature (500 °C), more chlorides are coordinated with Y(III) and hydration number decreases with more Cl⁻ complexes for a given P-T condition, different complexes were observed from MD simulations in each box. This reflects the different Y:Cl ratios in the boxes, but also the fact that the simulations in each box at the same P-T condition were started from different initial configurations, and due to the short time range of MD relative to ligand exchange rates, the final species detected from MD could be meta-stable.

3.2 XAS data refinement

3.2.1 XANES

XANES spectra are mainly a function of the oxidation state of the target atom, and the atomic number (e.g. O versus Cl) and geometrical arrangement of the ligands coordinated to the target atom. The edge position (red-shifted as the formal charge on the target atom decreases) and intensity of the white line (most intense band at the

edge position) can change as the ligands vary depending on composition and temperature (Bunker, 2010, Penner-Hahn, 2005; Etschmann, et al., 2017).

Yttrium XANES spectra show the classic “dehydration” effect with increasing temperature and salinity (e.g. Brugger et al., 2016). This is reflected by a decrease of the white line intensity and a shift to lower energy of the edge position, as shown in Figure 4 where the spectra obtained on Sol3 (0.01 m YCl_3) and Sol5 (9.5 m LiCl + 0.5 m HCl) at 25 and 400 °C are compared. The effect of increasing temperature and salinity combine so that the decrease of the white line intensity and energy shift are more pronounced for Cl-rich Sol5. Note that that the small energy shift is more clearly observed in the first derivative of the XANES spectra (Fig 4(b)).

Figure 4. XANES on highest Cl solutions

The qualitative discussion above was supported using *ab initio* XANES simulations. As shown in Figure 6(a), the positions of the spectral features are well reproduced by the calculations for the $\text{Y}_2\text{O}_3(\text{s})$ standard, except for the band at ~65.9 eV, which is shifted by ~8 eV. The relative intensities are well reproduced, but the total intensity of the white line is lower in the simulations than in the experiments. Figure 6(b) explores the shifts of the spectral features resulting from changes in bond distance and angles in a high symmetry $[\text{YO}_8]$ moiety. The angle affects the shape of the white line (intensity ratio of the two main bands contributing to the white line), and the bond distance causes a shift in the position of the white line. The MD structures -and most likely the real species in solution- reflect dynamic distortions of

the antiprism structure, which results in the small but significant differences in calculated XANES spectra (Figure 6(c)). In order to account for this, we calculated the averages from ≥ 50 frames over the simulation times for a number of simulations (Figure 6(d)). In general, the results of FDMNES of MD boxes and experiments agree. Importantly, the effects of temperature and salinity on the spectra are well reproduced by the simulations. It is noticeable that the Y-O distance at room temperature from MD and XAS is 2.42 Å and 2.37 Å, respectively; therefore, minor discrepancies between the spectra from FDMNES of MD boxes and spectra from experiments are reasonable.

Figure 6. XANES from FDMNES.

3.2.2 EXAFS

EXAFS spectra represent a final state interference effect arising from the scattering of the outgoing photoelectron from neighboring atoms, and are therefore mainly sensitive to the nature (atomic number), quantity and distance of the neighboring atoms.

The amplitude reduction factor (S_0^2) accounts for processes that contribute to the X-ray absorption coefficient but not to the EXAFS (Roy et al. 1997), and is determined by fitting a compound with similar molecular structure as the unknown. In our case, S_0^2 was determined by fixing the coordination of a low salinity solution, Sol6 (0.75 m HCl) at 30 °C to eight oxygen atoms, because the structure of the Y(III) aqua ion has been well characterized by previous studies (Ikeda et al., 2005a; Ohta et

al., 2008; Liu, X. et al., 2012; Lindqvist-Reis et al., 2000). A S_0^2 value of 0.73 was determined by refining the S_0^2 , bond lengths and EXAFS Debye-Waller factors for this solution; this value is consistent with theoretical constraints (Roy et al. 1997) and was used in all subsequent refinements.

The YOCl(s) structure (Zachariasen, 1949, ICSD # 31667) was used to generate the O and Cl paths. For each solution, all spectra were fitted simultaneously, resulting in one ΔE_0 and one set of goodness-of-fit parameters for each solution (Table 5). The total ligand number (one oxygen path and one chlorine path) was restrained to be between 6 and 8; attempts to decrease the minimum coordination number to 5 resulted in statistically inferior fits. The Debye-Waller σ^2 was fitted at 25 °C for each solution, with the constraint that it should then double from 30 to 500 °C, as determined from MD simulations. Note that the Debye-Waller values determined from the *ab initio* MD simulations are higher than the experimental ones, as a result of the short sampling times in *ab initio* MD, that tend to overestimate structural disorder. However, the relative changes in fitted Debye-Waller values are likely to be accurate, especially since the vibrational characteristics of the complexes are well reproduced by *ab initio* MD (e.g. Mei et al. 2013b and references therein). In practice this was applied by increasing the EXAFS Debye-Waller by a factor of 1.2 for each ~100 °C increase in temperature. The EXAFS Debye-Waller for Cl⁻ was defined to be the same as that for O, in part to reduce the number of variables and in part due to the (usually) low Cl:O ratio.

The Y k-space and Fourier transformed (R-space) EXAFS data are shown in [Figure 5](#) and the fit results are tabulated in [Table 5](#). As a general rule, the data show a small shift in k-space with increasing temperature. In R-space, the magnitude of the peak in the radial distribution function decreases, and the peak position shifts to a longer distance with increasing temperature, consistent with decreasing total coordination numbers and increasing Cl:O ratio. This evolution is also seen in the fitted structural parameters ([Table 5](#)): the largest change is recorded in Sol5 (9.5 m LiCl+0.5 m HCl), where the total ligand number decreased from 7.6 (30 °C) to 6.0 (450 °C), with the Cl:O ratio increasing from 0.0 to 1.0. Attempts were made to increase the Cl:O ratio to 2, i.e. 4xCl+2xO, in-line with the results from MD, however this skewed the fit peak significantly, resulting in a poor overall fit to the data.

[Figure 5. EXAFS](#)

[Table 5 EXAFS result](#)

In contrast, the total coordination number does not decrease as much in low salinity solutions, e.g. from 8 to 7 (Sol3, 30 to 400 °C) and 8 to 7.7 (Sol6, 30 to 400 °C), while the Cl:O ratio increases from 0 to ~0.6 and ~0.4 (Sol6 and Sol3 respectively).

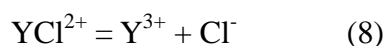
3.3 Estimating formation constants by *ab initio* thermodynamic integration

The MD simulations described above provided qualitative information about the nature and geometry of the Y-Cl complexes in chloride solutions to 500 °C. However,

thermodynamic properties of Y-Cl complexes are necessary to determine their relative stabilities and the mobility of Y(III) under hydrothermal conditions.

Figure 7. FES of YCl^{2+}

Figure 7 shows an example of employing *ab initio* MD to calculate the free energy surface of the reaction:



The Helmholtz free energy $\Delta A_{I \rightarrow II}$ of reaction (8) was calculated by integrating the constraint mean force ($f(r)$) between Y^{3+} and Cl^- (equation (1)) from the equilibrium position (2.65 Å), which corresponds to the equilibrated Y(III)- Cl^- bond distance in the previous unconstrained MD simulations, to a non-interacting position (6.00 Å). An external force is required to eliminate the interactions between Y^{3+} and Cl^- to maintain the targeted Y(III)- Cl^- distance. When the Y(III)- Cl^- distance was between 3.1 Å and 3.55 Å, the absolute value of $f(r)$ varied from zero to a minimum of -45.14 kJ/mol·Å to near zero (3.32 kJ/mol·Å), and the free energy reached its maximum (23.50 kJ/mol), which means at this stage, one water molecule associated with yttrium, i.e. reaction (7) results in the replacement of one chloride ion by one water molecule. The mean constraint forces become positive at distances between 3.4 Å and 5.4 Å, which reflects the activation barrier of the ion exchange reaction. It can be seen from Figure 7 that when the Y(III)- Cl^- distance is beyond 4.5 Å, the constraint mean force is very small (9.01 kJ/mol·Å, 2.03 kJ/mol·Å, -2.69 kJ/mol·Å, and -9.45 kJ/mol·Å at distances of 4.5 Å, 4.9 Å, 5.4 Å, and 6 Å, respectively), as expected as chloride-Y(III)

interaction become vanishingly small. The integration of the Y(III)-Cl⁻ mean constraint force over the reaction path gives a free energy for reaction (7) of 3.92 ± 8.85 kJ/mol.

Figure 8. free energy surface of all calculation

Figure 8 shows the free energy surface of the stepwise dissociation of Y(III)-chloride complexes in solutions with different Cl⁻ concentrations (box 1 and 3) at 200 °C, 800 bar; 350 °C, 800 bar; and 500 °C, 1000 bar. In order to achieve good sampling of the constraint force, one more free chloride was set in the system at a far distance (6 Å) to conduct thermodynamic integration, i.e. in box 1, which contains three Cl⁻, the free energies of formation of YCl_n³⁻ⁿ complexes were calculated only when n=1 and 2; in box 3, which contains five Cl⁻, Δ_rG of YCl_n³⁻ⁿ (n = 1,2,3,4) were measured (Table 6).

Table 6. ΔG and logK^Θ of two boxes

Comparing results from box 1 and box 3, the calculated Δ_rG for the association reactions of YCl²⁺ and YCl₂⁺ vary because of the difference of Cl⁻ activity in each box. After activity correction, the value of standard Gibbs free energies (Δ_rG^Θ) of each ligand exchange reaction were close (four are ≤2.2 kJ/mol, and two ≤3.8 kJ/mol) at the same P-T condition. The stepwise formation constants, logK^Θ, that were obtained from the two boxes at each P-T condition, their errors and averages are presented in Figure 9. The consistency of the two logK^Θ values from the two boxes validates the thermodynamic integration method for calculating the energetics of these ligand

exchange reactions, demonstrating that the values do not depend on the composition or size of the simulation box, and that the sampling time of the simulations is sufficient. In this study, we take the average stepwise formation constant of the two boxes as the final stepwise formation constant of the YCl^{2+} and YCl_2^+ association reactions at 200 °C, 800 bar; 350 °C, 800 bar; and 500 °C, 1000 bar. The error of the average formation constant was measured using the standard propagation rules. The stepwise ($\log K^\ominus$) and cumulative ($\log \beta^\ominus$) formation constants of Y(III)-chloride complexes are summarized in [Tables 6 and 7, respectively](#).

[Figure 9](#). average $\log K^\ominus$ and each $\log K^\ominus$ within error bar in different boxes with T.

[Table 7](#). $\log \beta$ of Y(III)-Cl.

The calculated $\log \beta$ in [Table 7](#) are employed to fit the modified MRB model ([eq. 6](#)) to extrapolate the formation constant of Y(III)-Cl⁻ associate reactions to higher temperature and pressure. We fit two parameters in [equation \(6\)](#) for each species to minimize the uncertainties. The $\log \beta_{(25^\circ\text{C}, 1 \text{ bar})}^\ominus$ of YCl^{2+} was chosen from Luo & Byrne ([2001](#)), which is the only available experiment data of Y(III)-Cl complexes, two parameters (*A* and *B*) were fitted; but for YCl_2^+ , YCl_3 , and YCl_4^- , the $B_{(zz/a)}$ are set to zero, and $\log \beta_{(25^\circ\text{C}, 1 \text{ bar})}^\ominus$ and the *A* parameter were fitted. The fitted MRB parameters are listed in [Table 8](#). The extrapolated logarithm of formation constants of Y(III)-Cl complexes at 25 °C to 500 °C, saturated pressure (P_{sat}) to 5000 bar from MRB, are listed in [Table 9](#).

[Table 8](#). MRB parameters

Table 9. log β from MRB

4 Discussion

4.1 Stability of Y(III)-Cl complexes

In general, the speciation derived from the unconstrained MD (section 3.1) agrees well with XAS fits (section 3.2) (Figures 10 and 11). The XANES spectra calculated from *first principles* from the MD simulations reproduce the experimental spectral features and their changes with temperature and salinity well (Figure 6d). The experiments and theoretical approaches both reveal the same trends of Y(III)-Cl complexes along with temperature, with more Cl⁻ bonding with Y(III) at high temperatures.

Figure 10. Coordination of O and Cl from XAS and MD

The formation constants obtained from thermodynamic integration enable us to predict Y(III)-Cl⁻ speciation at different PT and Cl⁻ concentrations and provide the first self-consistent speciation model for Y(III) chloride complexing from room-temperature to high-temperature hydrothermal conditions. The results indicate that the formation of Y(III)-chloride complexes can affect the mobility of yttrium under hydrothermal conditions and also the distribution of REE elements in REE deposits.

Figure 11 shows the distribution of Y(III) chloride complexes at different T, P and pH, as a function of total chloride in the solution. The number of coordinated chloride ligands from XAS Sol3 (0.03 m Cl⁻), Sol5 (2.5 m Cl⁻) and Sol7 (5 m Cl⁻) are

also plotted in [Figures 11a,c](#) and [11d,e,f](#) for comparison (right axis, orange dots). At 200 °C and $\text{pH}_{200^\circ\text{C}} = 0.3$ and 3, the hydrated Y^{3+} ion remains the dominant form of Y(III) even in high salinity solutions ([Figure 11a,b](#)). At 350 °C, the stability of the different species not only varies with Cl^- concentrations, but also with pH, so that the predominant species remains $\text{YCl}_3(\text{aq})$ from $n(\text{Cl}^-) > 0.4 \text{ m}$ at $\text{pH}_{350^\circ\text{C}} = 0.3$, but changes to YCl_4^- at $\text{pH}_{350^\circ\text{C}} = 3$. At 500 °C, 1000 bar ([Figure 11e,f](#)), the dominant species is YCl_4^- for $\text{pH}_{350^\circ\text{C}} = 3$, and $\text{YCl}_3(\text{aq})$ for $\text{pH}_{350^\circ\text{C}} = 0.3$. The coordination number of Cl^- is also 3 in XAS Sol 5 at 450 °C, whose Cl^- concentration is 10 m but also with high acidity. This decrease of Cl neighbors is likely due to the association of HCl at high temperature ([Mei et al., 2018](#); [Tagirov et al., 1997](#)) that leaves less free Cl^- available to bond with Y(III) in very acidic solutions.

While the general trends defined by (i) XAS, (ii) unconstrained MD ([Figure 10](#)) and (iii) thermodynamic modelling ([Figure 11](#)) derived from thermodynamic integration are consistent with each other, small discrepancies in the coordination number between the methods are noticeable. For example, at 200 °C, both unconstrained MD and the thermodynamic model indicate that there are Cl^- bonding with Y(III) when $n(\text{Cl}^-) > 2.5 \text{ m}$ (1 to 2 in MD and ~ 0.5 in the thermodynamic model), whereas XAS analysis reveals very minor chlorine complexation in Sol 7 and no chlorine complexation in Sol 6 ([Table 5 Sol6](#)) (i.e., below detection limit of $\sim 0.3 \text{ Cl}^-$). At 350 °C, the thermodynamic model suggests higher order Y(III)-Cl species than MD and XAS. This is because:

(1) thermodynamic integration with the MD method tends to overestimate the formation constants of complexes, and especially higher order complexes, at relative low temperature due to the low kinetic energy of the ions and water molecules, resulting in poor sampling of the force (Mei, et al., 2018). This translates into larger errors on the $\log\beta$ values at 25 °C than at 300 °C, for example (Mei et al., 2013a, 2015a). Therefore, the $\log\beta$ of Y(III)-Cl species at 200 and 350 °C from MD that was employed to model Y(III)-Cl distribution in this study could still be higher than actual, and consequently leads to the overestimation of the coordination of Y(III)-Cl. (2) As discussed above, due to the limits of CPU resources, the simulation time of unconstrained MD is not sufficient to observe the stable species, so species reported in Figure 10 could be meta-stable. (3) The experimental solutions are more acidic than those in the simulations, and HCl association could explain the lower Y-Cl bonding compared to other solutions and to the MD simulations (Fig. 11).

Overall, Y(III) mobility in hydrothermal conditions is expected to increase because of the increased stability of higher-order Y(III)-Cl with increasing temperature and Cl^- concentration.

Figure 11. Y-Cl species with $n(\text{Cl}^-)$ at different T and pH

4.2 REE- Cl^- complexation in hydrothermal fluids

The Y^{3+} ionic radius is close to that of Ho^{3+} , and Y has consequently frequently been grouped with heavy REE. However, differences in their aqueous speciation has

the potential to lead to different mobility of the REE and Y in natural hydrothermal systems. Up to now, this possibility could not be investigated due to the lack of thermodynamic properties for Y(III)-Cl complexes (Migdisov et al., 2016). The formation constants of YCl^{2+} and YCl_2^+ at 150, 200 and 250 °C, and P_{sat} have been derived from the fitted MRB parameters of Y(III)-Cl complexes (Table 9) and can now be compared to other REE data (Table 1, Migdisov et al., 2009) (Figure 12). At 150 °C, the formation constant for YCl^{2+} is close to zero, much smaller than those reported by Migdisov et al. (2016) for REECl^{2+} , even when considering the heaviest REE (Lu, which is 1.14). At 200 °C, yttrium behaves similar to the heavy REE (HREE) element (Lu) in Cl-rich solutions. In this condition, the LREE are more stable in solution and mobile than HREE, including Y(III). Nevertheless, the formation constants of Y-Cl complexes increase faster than those of other HREE with increasing temperature, so that at 250 °C Y(III)-Cl complexes are more stable than HREE, and Y behaves more like the LREE (La).

Figure 12. Compare of $\log\beta$ of REE & Y values

Differences between Y and the HREE thermodynamics under hydrothermal conditions provide a likely explanation for the fractionation of Y from Ho reported in some hydrothermal REE minerals (Bau and Dulski, 1995). The distribution of Ho(III) and Y(III) species as a function of Cl^- concentration at 250 °C, P_{sat} are presented in Figure 13, with the data presented in Table 9 for Y(III) and measured by Migdisov et al (2009) for Ho^{3+} , HoCl_2^+ and HoCl^{2+} , and predicted from Haas et al. (1995) for

HoCl₃(aq). As thermodynamic data for Ho(III) are only available until trichloro complexes, YCl₄⁻ is not considered in Figure 13. At 250 °C, the dominant species for Y(III) in Cl-bearing solution is YCl₂⁺, whereas for Ho(III), it remains HoCl²⁺ until Cl⁻ concentration reaches ~4.5 m and becomes HoCl₂⁺ afterwards. Such slight differences could ultimately account for contrasting REE(Y) distribution in hydrothermal REE deposits. However, the minerals deposited from hydrothermal fluids contain many components, i.e. F⁻, SO₄²⁻, CO₃²⁻. The behaviors of REE with most of these ligands are unclear but can affect the process of precipitation; therefore, further studies are required to quantitatively model how REE minerals deposits in hydrothermal process.

Figure 13. Y-Cl/Ho-Cl species distribution with Cl⁻ concentration at 250 °C, P_{sat}

Acknowledgements

We are grateful to the Australian Research Council (discovery grant DP190100216) for supporting this work. The MD part of this work was supported by resources provided by the Pawsey Supercomputing Centre with funding from the Australian Government and the Government of Western Australia and the high-performance computers in CSIRO. We are grateful to the European Synchrotron Research Facility (Grenoble, France) for providing beamtime, and to the Australian International Synchrotron Access Program (ISAP) managed by the Australian Synchrotron, part of ANSTO, and funded by the Australian Government, for travel funding. M. Louvel also acknowledges funding from the European Union's Horizon 2020 Marie Skłodowska-Curie grant DLV-797145.

Research data

Relevant research data are in attached spreadsheet.

References

- Allen, M. and Tildesley, D. (1987) *Computer Simulation of Liquids* Oxford Univ. Press. Oxford.
- Allen, P.G., Bucher, J.J., Shuh, D.K., Edelstein, N.M. and Craig, I. (2000) Coordination Chemistry of Trivalent Lanthanide and Actinide Ions in Dilute and Concentrated Chloride Solutions. *Inorganic Chemistry* 39, 595-601.
- Bankura A., Karmakar A., Carnevale V., Chandra A. and Klein 1064 M. L. (2014) Structure, dynamics, and spectral diffusion of water from first-principles molecular dynamics. *Journal of Physycal Chemistry* 1066 C 118, 29401–29411.
- Bau, D. (1995) Comparative study of yttrium and rare-earth element behaviours in fluorine-rich hydrothermal fluids. *Contrib Mineral petrol* 119, 213-223.
- Becke, A.D. (1988) Density-functional exchange-energy approximation with correct asymptotic behavior. *Phys. Rev. A* 38, 3098-3100.
- Bowron, D.T. and Diaz-Moreno, S. (2007) Local Structure Refinement of Disordered Material Models: Ion Pairing and Structure in YCl_3 Aqueous Solutions. *The Journal of Physical Chemistry B* 111, 11393-11399.
- Brugger, J. (2007a) BeerOz, a set of Matlab routines for the quantitative interpretation of spectrophotometric measurements of metal speciation in solution. *Computers & Geosciences* 33, 248-261.
- Brugger, J., Etschmann, B., Liu, W., Testemale, D., Hazemann, J.-L., Emerich, H., Van Beek, W. and Proux, O. (2007b) An XAS study of the structure and thermodynamics of Cu (I) chloride complexes in brines up to high temperature (400 C, 600 bar). *Geochimica et Cosmochimica Acta* 71, 4920-4941.
- Brugger, J., Etschmann, B., Pownceby, M., Liu, W., Grundler, P. and Brewe, D. (2008) Oxidation state of europium in scheelite: Tracking fluid–rock interaction in gold deposits. *Chemical Geology* 257, 26-33.
- Brugger, J., Liu, W., Etschmann, B., Mei, Y., Sherman, D.M. and Testemale, D. (2016) A review of the coordination chemistry of hydrothermal systems, or do coordination changes make ore deposits? *Chemical Geology* 447, 219-253.
- Bruyère, R., Prat, A., Goujon, C. and Hazemann, J.-L. (2008) A new pressure regulation device using high pressure isolation valves, *Journal of Physics: Conference Series*. IOP Publishing, p. 122003.

678 Bunker, G. (2010) Introduction to XAFS: a practical guide to X-ray absorption fine structure
679 spectroscopy. Cambridge University Press.

680 Bunău, O. and Joly, Y. (2012) Full potential x-ray absorption calculations using time
681 dependent density functional theory. *Journal of Physics: Condensed Matter* 24, 215502.

682 Campbell, L., Rehr, J.J., Schenter, G.K., McCarthy, M.I. and Dixon, D. (1999) XAFS
683 Debye–Waller factors in aqueous Cr³⁺ from molecular dynamics. *Journal of*
684 *Synchrotron Radiation* 6, 310-312.

685 Car, R. and Parrinello, M. (1985) Unified Approach for Molecular Dynamics and
686 Density-Functional Theory. *Phys. Rev. Lett.* 55, 2471-2474.

687 Chantler, C.T. (1995) Theoretical form factor, attenuation, and scattering tabulation for Z=
688 1–92 from E= 1–10 eV to E= 0.4–1.0 MeV. *Journal of Physical and Chemical Reference*
689 *Data* 24, 71-643.

690 Cossy, C., Helm, L. and Merbach, A.E. (1989) High-pressure NMR study. 38.
691 Water-exchange mechanisms on the terbium to thulium octa-aqua lanthanide(III) ions: a
692 variable-pressure oxygen-17 NMR study. *Inorganic Chemistry* 28, 2699-2703.

693 D'Angelo, P. and Spezia, R. (2012) Hydration of lanthanoids(III) and actinoids(III): an
694 experimental/theoretical saga. *Chemistry* 18, 11162-11178.

695 Díaz-Moreno, S., Muñoz-Páez, A. and Chaboy, J. (2000) X-ray Absorption Spectroscopy
696 (XAS) Study of the Hydration Structure of Yttrium(III) Cations in Liquid and Glassy
697 States: Eight or Nine-Fold Coordination? *The Journal of Physical Chemistry A* 104,
698 1278-1286.

699 Driesner, T. (2007) The system H₂O–NaCl. Part II: Correlations for molar volume, enthalpy,
700 and isobaric heat capacity from 0 to 1000°C, 1 to 5000bar, and 0 to 1 XNaCl.
701 *Geochimica et Cosmochimica Acta* 71, 4902-4919.

702 Driesner, T. and Heinrich, C.A. (2007) The system H₂O–NaCl. Part I: Correlation formulae
703 for phase relations in temperature–pressure–composition space from 0 to 1000°C, 0 to
704 5000bar, and 0 to 1 XNaCl. *Geochimica et Cosmochimica Acta* 71, 4880-4901.

705 Etschmann, B., Liu, W., Testemale, D., Mueller, H., Rae, N., Proux, O., Hazemann, J.-L. and
706 Brugger, J. (2010) An in situ XAS study of copper (I) transport as hydrosulfide
707 complexes in hydrothermal solutions (25–592 C, 180–600 bar): speciation and solubility
708 in vapor and liquid phases. *Geochimica et Cosmochimica Acta* 74, 4723-4739.

709 Etschmann, B., Liu, W., Li, K., Dai, S., Reith, F., Falconer, D., Kerr, G., Paterson, D.,
710 Howard, D. and Kappen, P. (2017) Enrichment of germanium and associated arsenic and
711 tungsten in coal and roll-front uranium deposits. *Chemical Geology* 463, 29-49.

712 Etschmann, B.E., Mei, Y., Liu, W., Sherman, D., Testemale, D., Müller, H., Rae, N., Kappen,
713 P. and Brugger, J. (2018) The role of Pb(II) complexes in hydrothermal mass transfer:
714 An X-ray absorption spectroscopic study. *Chemical Geology* 502, 88-106.

715 Etschmann, B., Liu, W., Mayanovic, R., Mei, Y., Heald, S., Gordon, R. and Brugger, J.
 716 (2019) Zinc transport in hydrothermal fluids: On the roles of pressure and sulfur vs.
 717 chlorine complexing. *American Mineralogist* 104, 158-161.

718 Gammons, C.H., Wood, S.A. and Williams-Jones, A.E. (1996) The aqueous geochemistry of
 719 the rare earth elements and yttrium: VI. Stability of neodymium chloride complexes
 720 from 25 to 300°C. *Geochimica et Cosmochimica Acta* 60, 4615-4630.

721 Gillan, M.J., Alfè, D. and Michaelides, A. (2016) Perspective: How good is DFT for water?
 722 *The Journal of Chemical Physics* 144, 130901.

723 Gysi, A.P., Williams-Jones, A.E. and Harlov, D. (2015) The solubility of xenotime-(Y) and
 724 other HREE phosphates (DyPO₄, ErPO₄ and YbPO₄) in aqueous solutions from 100
 725 to 250 °C and p sat. *Chemical Geology* 401, 83-95.

726 Helgeson, H.C. and Kirkham, D.H. (1974) Theoretical prediction of the thermodynamic
 727 behavior of aqueous electrolytes at high pressures and temperatures; II, Debye-Huckel
 728 parameters for activity coefficients and relative partial molal properties. *American*
 729 *Journal of Science* 274, 1199-1261.

730 Helgeson, H.C., Kirkham, D.H. and Flowers, G.C. (1981) Theoretical prediction of the
 731 thermodynamic behavior of aqueous electrolytes by high pressures and temperatures; IV,
 732 Calculation of activity coefficients, osmotic coefficients, and apparent molal and
 733 standard and relative partial molal properties to 600 degrees C and 5kb. *American*
 734 *Journal of Science* 281, 1249-1516.

735 Helm, L. and Merbach, A.E. (2005) Inorganic and Bioinorganic Solvent Exchange
 736 Mechanisms. *Chem. Rev.* 105, 1923-1960.

737 Humphrey, W., Dalke, A. and Schulten, K. (1996) VMD: Visual molecular dynamics. *Journal*
 738 *of Molecular Graphics* 14, 33-38.

739 Ikeda, T., Hirata, M. and Kimura, T. (2005a) Hydration of Y³⁺ ion: A Car-Parrinello
 740 molecular dynamics study. *The Journal of Chemical Physics* 122, 024510.

741 Ikeda, T., Hirata, M. and Kimura, T. (2005b) Hydration structure of Y³⁺ and La³⁺
 742 compared: An application of metadynamics. *The Journal of chemical physics* 122,
 743 244507.

744 Johansson, g. and Wakita, H. (1985) X-ray investigation of the coordination and complex
 745 formation of lanthanoid ions in aqueous perchlorate and selenate solutions. *Inorganic*
 746 *Chemistry* 24, 3047-3052.

747 Joly, Y. (2001) X-ray absorption near-edge structure calculations beyond the muffin-tin
 748 approximation. *Phys. Rev. B* 63, 125120.

749 Joly, Y., Bunău, O., Lorenzo, J.E., Galéra, R.M., Grenier, S. and Thompson, B. (2009)
 750 Self-consistency, spin-orbit and other advances in the FDMNES code to simulate
 751 XANES and RXD experiments. *Journal of Physics: Conference Series* 190, 012007.

752 Kontonikas-Charos, A., Ciobanu, C.L., Cook, N.J., Ehrig, K., Ismail, R., Krneta, S. and Basak,
 753 A. (2018) Feldspar mineralogy and rare-earth element (re)mobilization in iron-oxide

754 copper gold systems from South Australia: a nanoscale study. *Mineral. mag.* 82,
755 S173-S197.

756 Krause, M. O., & Oliver, J. H. (1979). Natural widths of atomic K and L levels, K α X- ray
757 lines and several KLL Auger lines. *Journal of Physical and Chemical Reference*
758 *Data*, 8(2), 329-338.

759 Krishnamurthy, N., Gupta, C.K. and Gupta, C.K. (2015) *Extractive Metallurgy of Rare Earths*.
760 CRC Press.

761 Lee, C., Yang, W. and Parr, R.G. (1988) Development of the Colle-Salvetti
762 correlation-energy formula into a functional of the electron density. *Phys. Rev. B* 37,
763 785-789.

764 Lemmon, E.W., McLinden, M.O. and Friend, D.G. (2000) *Thermophysical properties of fluid*
765 *systems*. National Institute of Standards and Technology, Gaithersberg.

766 Lin, I.C., Seitsonen, A.P., Tavernelli, I. and Rothlisberger, U. (2012) Structure and dynamics
767 of liquid water from ab initio molecular dynamics - comparison of BLYP, PBE and
768 revPBE density functionals with and without van der Waals corrections. *Journal of*
769 *Chemical Theory and Computation* 8, 3902-3910.

770 Lindqvist-Reis, P., Lamble, K., Pattanaik, S., Persson, I. and Sandström, M. (2000) Hydration
771 of the Yttrium(III) Ion in Aqueous Solution. An X-ray Diffraction and XAFS Structural
772 Study. *The Journal of Physical Chemistry B* 104, 402-408.

773 Ling, M.-X., Liu, Y.-L., Williams, I.S., Teng, F.-Z., Yang, X.-Y., Ding, X., Wei, G.-J., Xie,
774 L.-H., Deng, W.-F. and Sun, W.-D. (2013) Formation of the world's largest REE deposit
775 through protracted fluxing of carbonatite by subduction-derived fluids. *Sci Rep* 3, 1776.

776 Liu, W., Borg, S.J., Testemale, D., Etschmann, B., Hazemann, J.-L. and Brugger, J. (2011)
777 Speciation and thermodynamic properties for cobalt chloride complexes in hydrothermal
778 fluids at 35–440 C and 600 bar: an in-situ XAS study. *Geochimica et Cosmochimica*
779 *Acta* 75, 1227-1248.

780 Liu, X., Lu, X., Wang, R. and Zhou, H. (2012) First-principles molecular dynamics study of
781 stepwise hydrolysis reactions of Y3+ cations. *Chemical Geology* 334, 37-43.

782 Liu, W., Etschmann, B.E., Migdisov, A., Boukhalfa, H., Testemale, D., Muller, H., Hazemann,
783 J.-L. and Brugger, J., 2017. Revisiting the hydrothermal geochemistry of europium
784 (II/III) in light of new in-situ XAS spectroscopy results. *Chemical Geology* 459, 61-74.

785 Loges, A., Migdisov, A.A., Wagner, T., Williams-Jones, A.E. and Markl, G. (2013) An
786 experimental study of the aqueous solubility and speciation of Y(III) fluoride at
787 temperatures up to 250°C. *Geochimica et Cosmochimica Acta* 123, 403-415.

788 Louvel, M., Bordage, A., Testemale, D., Zhou, L. and Mavrogenes, J., 2015. Hydrothermal
789 controls on the genesis of REE deposits: Insights from an in situ XAS study of Yb
790 solubility and speciation in high temperature fluids (T < 400 C). *Chemical Geology*
791 417, 228-237.

792 Louvel, M., Bordage, A., Tripoli, B., Testemale, D., Hazemann, J.-L. and Mavrogenes, J.,
793 2017. Effect of S on the aqueous and gaseous transport of Cu in porphyry and

794 epithermal systems: Constraints from in situ XAS measurements up to 600 °C and 300
795 bars. *Chemical Geology* 466, 500-511.

796 Luo, Y.-R. and Byrne, R.H. (2001) Yttrium and Rare Earth Element Complexation by
797 Chloride Ions at 25°C. *Journal of Solution Chemistry*, 9.

798 Marques, M.I.d.B., Marques, M.A. and Rodrigues, J.R. (1992) The structure of the first
799 coordination shell of the yttrium ion in concentrated aqueous solutions of YBr
800 ₃ and YCl ₃. *Journal of Physics: Condensed Matter* 4,
801 7679-7690.

802 Marshall, W.L. and Franck, E.U. (1981) Ion product of water substance, 0–1000 °C, 1–10,000
803 bars New International Formulation and its background. *Journal of Physical and*
804 *Chemical Reference Data* 10, 295-304.

805 Matsubara, E., Okuda, K. and Waseda, Y. (1990) Anomalous X-ray scattering study of
806 aqueous solutions of YCl ₃ and ErCl ₃. *Journal of Physics:*
807 *Condensed Matter* 2, 9133-9143.

808 Mei, Y., Sherman, D.M., Liu, W. and Brugger, J. (2013a) *Ab initio* molecular dynamics
809 simulation and free energy exploration of copper(I) complexation by chloride and
810 bisulfide in hydrothermal fluids. *Geochimica et Cosmochimica Acta* 102, 45-64.

811 Mei, Y., Sherman, D.M., Liu, W. and Brugger, J. (2013b) Complexation of gold in S₃²⁻-rich
812 hydrothermal fluids: evidence from *ab-initio* molecular dynamics simulations. *Chemical*
813 *Geology*, 347, 34–42.

814 Mei, Y., Sherman, D.M., Liu, W., Etschmann, B., Testemale, D. and Brugger, J. (2015a) Zinc
815 complexation in chloride-rich hydrothermal fluids (25–600 °C): A thermodynamic
816 model derived from *ab initio* molecular dynamics. *Geochimica et Cosmochimica Acta*
817 150, 265-284.

818 Mei, Y., Etschmann, B., Liu, W., Sherman, D.M., Barnes, S.J., Fiorentini, M.L., Seward,
819 T.M., Testemale, D. and Brugger, J. (2015b) Palladium complexation in chloride- and
820 bisulfide-rich fluids: Insights from *ab initio* molecular dynamics simulations and X-ray
821 absorption spectroscopy. *Geochimica et Cosmochimica Acta* 161, 128-145.

822 Mei, Y., Etschmann, B., Liu, W., Sherman, D.M., Testemale, D. and Brugger, J. (2016)
823 Speciation and thermodynamic properties of zinc in sulfur-rich hydrothermal fluids:
824 Insights from *ab initio* molecular dynamics simulations and X-ray absorption
825 spectroscopy. *Geochimica et Cosmochimica Acta* 179, 32-52.

826 Mei, Y., Liu, W., Brugger, J., Sherman, D.M. and Gale, J.D. (2018) The dissociation
827 mechanism and thermodynamic properties of HCl(aq) in hydrothermal fluids (to 700 °C,
828 60 kbar) by *ab initio* molecular dynamics simulations. *Geochimica et Cosmochimica*
829 *Acta* 226, 84-106.

830 Migdisov, A.A. and Williams-Jones, A.E. (2008) A spectrophotometric study of Nd(III),
831 Sm(III) and Er(III) complexation in sulfate-bearing solutions at elevated temperatures.
832 *Geochimica Cosmochimica Acta* 72, 5291-5303.

833 Migdisov, A.A., Williams-Jones, A.E., Normand, C. and Wood, S.A. (2008) A
834 spectrophotometric study of samarium (III) speciation in chloride solutions at elevated
835 temperatures. *Geochimica Cosmochimica Acta* 72, 1611-1625.

836 Migdisov, A., Williams-Jones, A.E., Brugger, J. and Caporuscio, F.A. (2016) Hydrothermal
837 transport, deposition, and fractionation of the REE: Experimental data and
838 thermodynamic calculations. *Chemical Geology* 439, 13-42.

839 Migdisov, A.A., Williams-Jones, A.E. and Wagner, T. (2009) An experimental study of the
840 solubility and speciation of the Rare Earth Elements (III) in fluoride- and
841 chloride-bearing aqueous solutions at temperatures up to 300°C. *Geochimica et*
842 *Cosmochimica Acta* 73, 7087-7109.

843 Ohta, A., Kagi, H., Tsuno, H., Nomura, M. and Kawabe, I. (2008) Influence of multi-electron
844 excitation on EXAFS spectroscopy of trivalent rare-earth ions and elucidation of change
845 in hydration number through the series. *American Mineralogist* 93, 1384-1392.

846 Penner- Hahn, J.E. (2001) X- ray absorption spectroscopy. e LS.

847 Proux, O., Biquard, X., Lahera, E., Menthonnex, J.-J., Prat, A., Ulrich, O., Soldo, Y.,
848 Trévisson, P., Kapoujyan, G. and Perroux, G. (2005) FAME: A new beamline for X-ray
849 absorption investigations of very-diluted systems of environmental, material and
850 biological interests. *Physica Scripta* 2005, 970.

851 Ram, R., Becker, M., Brugger, J., Etschmann, B., Burcher-Jones, C., Howard, D., Kooyman,
852 P. and Petersen, J. (2019) Characterisation of a rare earth element (REE)-bearing
853 ion-adsorption clay deposit in Madagascar. *Chemical Geology* 522, 93-107.

854 Ravel, B. and Newville, M. (2005) ATHENA, ARTEMIS, HEPHAESTUS: data analysis for
855 X-ray absorption spectroscopy using IFEFFIT. *Journal of synchrotron radiation* 12,
856 537-541.

857 Rehr, J.J., Kas, J.J., Prange, M.P., Sorini, A.P., Takimoto, Y. and Vila, F. (2009) Ab initio
858 theory and calculations of X-ray spectra. *Comptes Rendus Physique* 10, 548-559.

859 Rodinger, T., Howell, P.L. and Pomès, R. (2005) Absolute free energy calculations by
860 thermodynamic integration in four spatial dimensions. *The Journal of chemical physics*
861 123, 034104.

862 Roy, M., Gurman, S.J. and vanDorssen, G. (1997) The amplitude reduction factor in EXAFS.
863 *Journal De Physique Iv* 7, 151-152. Rudolph, W.W. and Irmer, G. (2015) Hydration and
864 ion pair formation in aqueous Y^{3+} -salt solutions. *Dalton Transactions* 44, 18492-18505.

865 Ryzhenko, B., Bryzgalin, O., Artamkina, I.Y., Spasennykh, M.Y. and Shapkin, A. (1985) An
866 electrostatic model for the electrolytic dissociation of inorganic substances dissolved in
867 water. *Geochem. Int.* 22, 138-144.

868 Santos, C., Strecker, K., Suzuki, P.A., Kycia, S., Silva, O.M.M. and Silva, C.R.M. (2005)
869 Stabilization of α -SiAlONs using a rare-earth mixed oxide (RE₂O₃) as sintering additive.
870 *Materials Research Bulletin* 40, 1094-1103.

871 Shannon, R.D. (1976) Revised effective ionic radii and systematic studies of interatomic
872 distances in halides and chalcogenides. *Acta crystallographica section A: crystal physics,*
873 *diffraction, theoretical and general crystallography* 32, 751-767.

874 Sharps, J.A., Brown Jr, G.E. and Stebbins, J.F. (1993) Kinetics and mechanism of ligand
875 exchange of Au (III), Zn (II), and Cd (II) chlorides in aqueous solution: An NMR study
876 from 28–98 C. *Geochimica et cosmochimica acta* 57, 721-731.

877 Shvarov, Y.V. and Bastrakov, E. (1999) HCh: a software package for geochemical
878 equilibrium modelling. User's Guide Record/25 (Australian Geological Survey
879 Organisation, Canberra, 1999).

880 Shvarov, Y.V. (2008) HCh: New potentialities for the thermodynamic simulation of
881 geochemical systems offered by windows. *Geochem. Int.* 46, 834-839.

882 Shvarov, Y. (2015) A suite of programs, OptimA, OptimB, OptimC, and OptimS compatible
883 with the Unitherm database, for deriving the thermodynamic properties of aqueous
884 species from solubility, potentiometry and spectroscopy measurements. *Applied*
885 *Geochemistry* 55, 17-27.

886 Sprik, M., Hutter, J. and Parrinello, M. (1996) Ab initio molecular dynamics simulation of
887 liquid water: Comparison of three gradient-corrected density functionals. *The Journal of*
888 *chemical physics* 105, 1142-1152.

889 Sprik, M. and Ciccotti, G. (1998) Free energy from constrained molecular dynamics. *The*
890 *Journal of Chemical Physics* 109, 7737.

891 Sprik, M. (2000) Computation of the pK of liquid water using coordination constraints.
892 *Chemical Physics* 258, 139-150.

893 Stefanski, J. and Jahn, S.: Yttrium speciation in subduction zone fluids from ab
894 initio molecular dynamics simulations, *Solid Earth Discuss.*,
895 <https://doi.org/10.5194/se-2019-195>, in review, 2020.

896 Tagirov, B.R., Zotov, A.V. and Akinfiev, N.N. (1997) Experimental study of dissociation of
897 HCl from 350 to 500°C and from 500 to 2500 bars: Thermodynamic properties of
898 HCl°(aq). *Geochimica et Cosmochimica Acta* 61, 4267-4280.

899 Testemale, D., Argoud, R., Geaymond, O. and Hazemann, J.-L. (2005) High pressure/high
900 temperature cell for x-ray absorption and scattering techniques. *Review of Scientific*
901 *Instruments* 76, 043905.

902 Testemale, D., Brugger, J., Liu, W., Etschmann, B. and Hazemann, J.-L. (2009) In-situ X-ray
903 absorption study of Iron(II) speciation in brines up to supercritical conditions. *Chemical*
904 *Geology* 264, 295-310.

905 Tian, Y., Etschmann, B., Mei, Y., Grundler, P.V., Testemale, D., Hazemann, J.-L., Elliott, P.,
906 Ngothai, Y. and Brugger, J. (2014) Speciation and thermodynamic properties of
907 manganese(II) chloride complexes in hydrothermal fluids: In situ XAS study.
908 *Geochimica et Cosmochimica Acta* 129, 77-95.

- 909 Tu, Y.-J., Lin, Z., Allen, M.J. and Cisneros, G.A. (2018) Molecular dynamics investigation of
910 water-exchange reactions on lanthanide ions in water/1-ethyl-3-methylimidazolium
911 trifluoromethylsulfate ([EMIm][OTf]). *The Journal of Chemical Physics* 148, 024503.
- 912 Vala Ragnarsdottir, K., Oelkers, E.H., Sherman, D.M. and Collins, C.R. (1998) Aqueous
913 speciation of yttrium at temperatures from 25 to 340°C at Psat: an in situ EXAFS study.
914 *Chemical Geology* 151, 29-39.
- 915 Weng, Z., Jowitt, S.M., Mudd, G.M. and Haque, N. (2015) A Detailed Assessment of Global
916 Rare Earth Element Resources: Opportunities and Challenges. *Economic Geology* 110,
917 1925-1952.
- 918 Williams-Jones, A.E., Migdisov, A.A. and Samson, I.M. (2012) Hydrothermal Mobilisation
919 of the Rare Earth Elements - a Tale of "Ceria" and "Yttria". *Elements* 8, 355-360.
- 920 Wood, S.A. The aqueous geochemistry of the rare-earth elements and yttrium. 28.
- 921 Xing, Y., Etschmann, B., Liu, W., Mei, Y., Shvarov, Y., Testemale, D., Tomkins, A. and
922 Brugger, J. (2019) The role of fluorine in hydrothermal mobilization and transportation
923 of Fe, U and REE and the formation of IOCG deposits. *Chemical Geology* 504, 158-176.
- 924 Zachariasen, W. (1949) Crystal chemical studies of the 5f-series of elements. XII. New
925 compounds representing known structure types. *Acta Crystallographica* 2, 388-390.

Table 1 Structure of aqueous Y(III) at room temperature (~25 °C) and hydrothermal conditions in literature.

	Methods	conditions	hydration	Y-O distance (Å)	reference	note
Experimental studies	XRD	1.094 m Y(ClO ₄) ₃	8.0 ± 0.3	2.365	Johansson and Wakita, 1985	
	AXS	0.5 M YCl ₃	8.1 ± 0.3	2.51 ± 0.02	Matsubara et al., 1990	
	EXAFS	1 M YCl ₃	8.2 ± 0.5	2.46 ± 0.02		
		0.5 M YCl ₃	7.5	2.33	Marques et al., 1992	No Y-Cl bonds were found in either Raman and EXAFS
		1.0 M YCl ₃	8.5	2.33		
	EXAFS	1.2 M YCl ₃	7.5	2.34		
		(a) 0.1 M YCl ₃	9.1	2.36	Ragnarsdottir et al., 1998	No Y-Cl bonding and hydration decreases by 0.6, 2.6 and 1.8 with temperature increasing up to 340 °C for (a) and 250 °C for (b) and (c)
		(b) 0.1 M YCl ₃ + 0.23M HCl + 1M NaCl	10.2	2.36		
		(c) 0.1 M YCl ₃ + 0.23M HCl + 2M NaCl;	10.3	2.37		
	EXAFS&LXAS	1.71 M Y(ClO ₄) ₃ in HClO ₄	8	2.368 ± 0.003	Lindqvist-Reis et al., 2000	
	EXAFS	0.005 ~ 2 m YBr ₃	8	2.353 ± 0.001	Diaz-Moreno et al., 2000	
	EXAFS	0.1 M YCl ₃ + 0.25 M HCl/14 M LiCl	9.7/9.6		Allen et al., 2000	
	EXAFS & EPSR	1 m YCl ₃	7.5 ± 0.5	2.33	Bowron and Diaz-Moreno, 2007	0.8 ± 0.2 Y-Cl
	RAMAN/ DFT	3.2 M YCl ₃ and 2.03 M YCl ₃ + (0, 1, 4M HCl)	8-n	2.366	Rudolph and Irmer, 2015	Square antiprism, with <u>n</u> Y-Cl bonds (<u>n = 1,2</u>); n=0 when Cl ⁻ concentration < 0.2 m
Theoretical studies	DFT	1 m YCl ₃	8	2.38	Ikeda et al., 2005a, b	Square antiprism structure
	AIMD	1 Y ³⁺ in 63 waters' box	8		Liu et al., 2012	

Table 2. Simulation details of *ab initio* MD.

Box No.	Solution composition	Job No.	T (°C)	P (bar)	Box size (Å ³)	Density (g/cm ³)
1	55 H ₂ O, Y ³⁺ , 3Cl ⁻ (3 m Cl ⁻)	1a(1,2)	25	1	12.048	1.127
		1b	200	800	12.366	1.042
		1c	350	800	12.999	0.897
		1d	500	800	14.228	0.684
		1e	500	1000	13.940	0.727
2	55 H ₂ O, Y ³⁺ , 4 Cl ⁻ , 1 Na ⁺ (4 m Cl ⁻)	2a	200	800	12.443	1.073
		2b	350	800	13.032	0.934
		2c	500	1000	14.122	0.734
3	55 H ₂ O, Y ³⁺ , 5 Cl ⁻ , 2 Na ⁺ (5 m Cl ⁻)	3a	200	800	12.526	1.101
		3b	350	800	13.085	0.966
		3c	500	1000	13.865	0.812
4	111 H ₂ O, Y ³⁺ , 5 Cl ⁻ , 1 Na ⁺ , H ⁺ (2.5 m Cl ⁻)	4a	200	800	15.577	1.006
		4b	350	800	16.412	0.860
		4c	450	800	17.368	0.726

Table 3. XAS solution compositions.

Sample composition	Serial Number	condition
0.01 m YCl_3 + 0.75 m HCl	Sol 6	30 °C – 400 °C, 800 bar
0.01 m YCl_3 + 10 m LiCl + 0.5 m HCl	Sol 5	30 °C – 450 °C, 800 bar
0.01 m YCl_3 + 2 m NaCl + 0.5 m HCl	Sol 7	30 °C – 350 °C, 800 bar
0.01 m YCl_3 + 1 drop HCl	Sol 3	30 °C – 400 °C, 800 bar
1 m YCl_3	Sol 12	30 °C – 450 °C, 800 bar

Table 4. Simulation results by *ab initio* MD, error of coordination was measured from radial distribution function at distance range of 2.75 Å - 3.25 Å for Y-O and 2.9 Å – 3.2 Å for Y-Cl; Debye-Waller can only be measured when there is no ligand exchange in the simulation.

No	T (°C), P (bar)	Time (ps)	Initial configuration	Stable species	Y-Cl			Y-O			CN _{tot}
					N	r(Å)	σ^2 (Å ²)	N	r(Å)	σ^2 (Å ²)	
1a(1)	25, 1	25.37	[Y(H ₂ O) ₈] ³⁺	[Y(OH ₂) ₈] ³⁺				8	2.42	0.0106	8
1a(2)	25, 1	23.02	[Y(H ₂ O) ₇ Cl] ²⁺	[Y(OH ₂) ₈] ³⁺				8	2.42	0.0107	8
1b	200, 800	30.17	[Y(H ₂ O) ₆ Cl ₂] ⁺	[Y(H ₂ O) _{5.5} Cl _{1.8}] ^{1.2+}	1.7(0.1)	2.65		5.2(0.1)	2.36		7
1c	350, 800	23.87	[Y(H ₂ O) ₇ Cl ₂] ⁺	[Y(H ₂ O) _{4.5} Cl ₂] ⁺	2(0.1)	2.62	0.0172	4.5(0.1)	2.36		6.5
1d	500, 800	22.43	[Y(H ₂ O) ₅ Cl ₃] ⁰	[Y(OH ₂) ₃ Cl ₃] ⁰	3(0.2)	2.55	0.0155	3(0.2)	2.44		6
1e	500, 1000	26.94	[Y(H ₂ O) ₅ Cl ₃] ⁰	[Y(OH ₂) ₃ Cl ₃] ⁰	3	2.56	0.0200	3	2.44		6
2a	200, 800	20.30	[Y(H ₂ O) ₇ Cl ₂] ²⁺	[Y(H ₂ O) _{5.3} Cl _{1.8}] ^{1.2+}	1.8(0.1)	2.6		5.2(0.1)	2.35		7.1
2b	350, 800	19.21	[Y(H ₂ O) ₇ Cl ₂] ⁺	[Y(H ₂ O) ₅ Cl ₂] ⁺	1.9(0.1)	2.66	0.0236	4.9(0.2)	2.38		7
2c	500, 1000	16.23	[Y(H ₂ O) ₆ Cl ₂] ⁺	[Y(H ₂ O) _{4.2} Cl ₂] ⁺	2(0.1)	2.56		4.1(0.2)	2.33		6.2
3a	200, 800	16.06	[Y(H ₂ O) ₇ Cl] ²⁺	[Y(OH ₂) ₅ Cl ₂] ⁺	2(0.1)	2.67	0.0168	5(0.1)	2.38		7
3b	350, 800	17.52	[Y(OH ₂) ₄ Cl ₃] ⁰	[Y(OH ₂) _{3.9} Cl _{2.3}] ²⁺	2.3(0.1)	2.61		3.9(0.1)	2.35		6.2
3c	500, 1000	17.01	[Y(H ₂ O) ₃ Cl ₃] ⁰	[Y(OH ₂) ₂ Cl ₄] ⁻	4(0.1)	2.59	0.0194	1.7(0.3)	2.45		5.7
4a	200, 800	22.35	[Y(H ₂ O) ₈ Cl] ²⁺	[Y(H ₂ O) ₆ Cl] ²⁺	1	2.63	0.0116	6(0.1)	2.34	0.0155	7
4b	350, 800	16.92	[Y(OH ₂) ₅ Cl ₃] ⁰	[Y(OH ₂) _{3.7} Cl ₂] ⁺	2	2.63	0.0165	4.1(0.1)	2.36		6.1
4c	450, 800	16.91	[Y(OH ₂) ₅ Cl ₃] ⁰	[Y(OH ₂) ₃ Cl ₃] ⁰	3	2.56	0.0191	3.1(0.2)	2.37		6.1

Table 5. EXAFS results.

T (°C)	nO	rO	nCl	rCl	n _{tot} (first shell)	nY	rY	ss	k-range	R-range
Sol 6			E ₀ = 2.2(4)	$\chi^2_{\text{red}} = 661$	r-factor = 0.045					
30	8.0 (fix)*	2.369(7)			8	1 (fix)	4.78 (fix)	0.0041(8)	2<k<11	1.1<R<4.5
200	7.0(4)	2.391(8)	(1)		7	1 (fix)	4.78 (fix)	1.4*ssO1	2<k<11	1.1<R<4.5
300	6.4(1)	2.39(1)	0.6(5)	2.60 (fix)	7	1 (fix)	4.78 (fix)	1.6*ssO1	2<k<11	1.2<R<4.5
350	5.2(4)	2.36(1)	1.8(4)	2.68(2)	7	1 (fix)	3.94 (fix)	1.7*ssO1	2<k<10	1.2<R<4.5
400	4.4(4)	2.34(1)	2.6(4)	2.64(1)	7	1 (fix)	3.94 (fix)	1.8*ssO1	2<k<10	1.2<R<4.5
Sol 5			E ₀ = 3.3(4)	$\chi^2_{\text{red}} = 523$	r-factor = 0.037					
30	7.6(4)	2.388(7)			7.6	1 (fix)	4.74 (fix)	0.0023(3)	2<k<11	1.15<R<4.5
200	6.2(4)	2.398(8)	1.0 (fix)	2.66 (fix)	7.2	1 (fix)	4.74 (fix)	1.4*ssO1	2<k<9	1.15<R<4.5
300	4.0(2)	2.356(8)	2.0(1)	2.68(1)	6	1 (fix)	3.99 (fix)	1.6*ssO1	2<k<10	1.15<R<4.5
350	3.4(1)	2.331(1)	2.6(1)	2.652(9)	6	1 (fix)	3.99 (fix)	1.7*ssO1	2<k<10	1.15<R<4.5
400	3.0(3)	2.338(1)	3.0(1)	2.657(8)	6	1 (fix)	3.99 (fix)	1.8*ssO1	2<k<10	1.15<R<4.5
450	3.0 (fix)	2.326(1)	3.0 (fix)**	2.649(8)	6	1 (fix)	3.99 (fix)	1.9*ssO1	2<k<10	1.15<R<4.5
Sol 7			E ₀ = 2.2(4)	$\chi^2_{\text{red}} = 632$	r-factor = 0.043					
30	8.0(5)	2.362(8)			8	1 (fix)	4.78 (fix)	0.0041(6)	2<k<11	1.0<R<4.5
200	7.3(4)	2.389(8)	(1)		7.3	1 (fix)	4.78 (fix)	1.4*ssO1	2<k<11	1.0<R<4.5
300	5.8(4)	2.38(1)	1.5(4)	2.70(2)	7.3	1 (fix)	3.99 (fix)	1.6*ssO1	2<k<11	1.0<R<4.5
350	5.1(3)	2.36(1)	2.1(3)	2.67(1)	7.2	1 (fix)	3.99 (fix)	1.7*ssO1	2<k<11	1.0<R<4.5
Sol 3			E ₀ = 1.8(4)	$\chi^2_{\text{red}} = 673$	r-factor = 0.039					
30	8.0(1)	2.378(8)			8	1 (fix)	4.74 (fix)	0.0050(4)	2<k<11.5	1<R<4.5
200	7.8(3)	2.384(7)	(1)		7.8	1 (fix)	4.74 (fix)	1.4*ssO1	2<k<11	1<R<4.5
300	6.9(3)	2.38(1)	0.9(3)	2.69(6)	7.8	1 (fix)	3.99 (fix)	1.6*ssO1	2<k<11	1<R<4.5
350	6.4(4)	2.37(1)	1.3(4)	2.68(3)	7.7	1 (fix)	3.99 (fix)	1.7*ssO1	2<k<10	1<R<4.5
400	5.7(6)	2.34(1)	2.0(6)	2.64(3)	7.7	1 (fix)	3.99 (fix)	1.8*ssO1	2<k<9	1<R<4.5
Sol 12			E ₀ = 0.3(5)	$\chi^2_{\text{red}} = 7725$	r-factor = 0.031					
30	8.0(1)	2.374(6)			8	1 (fix)	4.74 (fix)	0.0042(4)	2<k<12	1.1<R<4.0
200	7.9(5)	2.364(7)	0.6(4)	2.60 (fix)	8.5	1 (fix)	4.74 (fix)	1.4*ssO1	2<k<12	1.1<R<4.0
300	6.2(4)	2.36(1)	1.6(4)	2.69(2)	7.8	1 (fix)	3.99 (fix)	1.6*ssO1	2<k<10	1.1<R<4.0

350	5.7(5)	2.36(1)	2.1(4)	2.67(2)	7.8	1 (fix)	3.99 (fix)	1.7*ssO1	2<k<10	1.1<R<4.0
400	5.2(5)	2.35(1)	2.6(5)	2.65(2)	7.8	1 (fix)	3.99 (fix)	1.8*ssO1	2<k<10	1.1<R<4.0
450	4.2(6)	2.35(2)	3.1(1)	2.64(2)	7.3	1 (fix)	3.99 (fix)	1.9*ssO1	2<k<10	1.1<R<4.0

NOTE: applied constraints, i.e. $n_{Cl} @ T_i \leq n_{Cl} @ T_{i+1}$, and $n_{tot} @ T_i \geq n_{tot} @ T_{i+1}$.

*fix based on everyone else's determination of $n=8$ at ambient conditions, use this to determine S_0^2 .

**Data at 450°C is noisier than at 400°C; equally good fits are obtained up to $n_{Cl} = 3.3$.

Table 6. Gibbs free energy of reactions and stepwise stability constants of Y(III)-Cl association reactions, calculated from box 1 and box 3. $\Delta_r G$, Gibbs free energy for the reaction; $\Delta_r G^{\ominus,c}$, Gibbs free energy at infinite dilution; $\Delta_r G^{\ominus}$, Gibbs free energy with concentration and activity correction.

Reaction in box 1	T(°C), P(bar)	$\Delta_r G$ (kJ/mol)	$\Delta_r G^{\ominus,c}$ (kJ/mol)	$\Delta_r G^{\ominus}$ (kJ/mol)	$\log K^{\ominus}$
$Y^{3+} + Cl^- = YCl^{2+}$	200, 800	-3.92 ± 8.85	3.60	-8.27	0.91 ± 0.98
	350, 800	-24.35 ± 10.42	-14.46	-55.96	4.69 ± 0.87
	500, 1000	-50.34 ± 11.60	-38.06	-146.44	9.89 ± 0.78
$YCl^{2+} + Cl^- = YCl_2^+$	200, 800	1.84 ± 9.21	7.30	-1.53	0.17 ± 1.01
	350, 800	-26.48 ± 10.11	-19.30	-45.33	3.80 ± 0.87
	500, 1000	-37.31 ± 11.37	-28.40	-93.27	6.30 ± 0.77
Reaction in box 3					
$Y^{3+} + Cl^- = YCl^{2+}$	200, 800	-12.05 ± 8.01	-2.21	-9.95	1.01 ± 0.89
	350, 800	-28.22 ± 9.48	-15.26	-58.19	4.88 ± 0.79
	500, 1000	-36.07 ± 10.06	-19.98	-142.58	9.63 ± 0.68
$YCl^{2+} + Cl^- = YCl_2^+$	200, 800	-2.12 ± 8.74	6.73	0.64	-0.07 ± 0.96
	350, 800	-26.23 ± 10.72	-14.58	-42.32	3.55 ± 0.90
	500, 1000	-30.62 ± 9.86	-16.16	-92.95	6.28 ± 0.67
$YCl_2^+ + Cl^- = YCl_3(aq)$	200, 800	2.70 ± 9.69	10.21	8.12	-0.90 ± 1.07
	350, 800	-12.19 ± 9.36	-2.30	-16.15	1.35 ± 0.78
	500, 1000	-33.39 ± 9.97	-21.12	-61.74	4.17 ± 0.67
$YCl_3(aq) + Cl^- = YCl_4^-$	200, 800	1.29 ± 8.46	6.75	6.75	-0.74 ± 0.93
	350, 800	-5.76 ± 9.15	1.42	1.42	-0.12 ± 0.77
	500, 1000	-17.84 ± 10.63	-8.93	-8.93	0.60 ± 0.72

Table 7. Cumulative formation constant of Y(III)-Cl complexes.

Reaction	T(°C), P(bar)	log β^0	<i>error</i>
$\text{Y}^{3+} + \text{Cl}^- = \text{YCl}^{2+}$	200, 800	0.96	0.66
	350, 800	4.79	0.59
	500, 1000	9.76	0.50
$\text{Y}^{3+} + 2 \text{Cl}^- = \text{YCl}_2^+$	200, 800	1.01	0.95
	350, 800	8.47	0.86
	500, 1000	16.05	0.71
$\text{Y}^{3+} + 3 \text{Cl}^- = \text{YCl}_3(\text{aq})$	200, 800	0.11	1.43
	350, 800	9.82	1.16
	500, 1000	20.22	0.98
$\text{YCl}_3(\text{aq}) + \text{Cl}^- = \text{YCl}_4^-$	200, 800	-0.63	1.71
	350, 800	9.70	1.39
	500, 1000	20.82	1.22

Table 8. Modified Ryzhenko–Bryzgalin (MRB) (Ryzhenko et al., 1985; Shvarov and Bastrakov, 1999) equation of state parameters for the Y(III)-Cl complexes obtained via fitting of $\log K^\ominus$ values from MD simulations. *The B parameters were set to zero, except for the association reaction of $Y^{3+} + Cl^- = YCl^{2+}$, whose $\log \beta_{(25^\circ C, 1 \text{ bar})}^\ominus$ was chosen from Luo & Byrne (2001). [you have K is italics sometimes...]

reaction	$\log \beta_{(25^\circ C, 1 \text{ bar})}^\ominus$	A_{zz}	B_{zz}^*
$Y^{3+} + Cl^- = YCl^{2+}$	0.65	3.357	- 1428
$Y^{3+} + 2 Cl^- = YCl_2^+$	-8.314	3.047	-
$Y^{3+} + 3 Cl^- = YCl_3(aq)$	-12.914	3.97	-
$Y^{3+} + 4 Cl^- = YCl_4^+$	-14.800	4.176	-

Table 9. the logarithm of formation constant Y(III)-Cl complexes calculated using MRB parameters in Table 8. *, values are used in discussion part.

T (° C)	P _{Sat}	800 bar	1000 bar	2000 bar	5000 bar	P _{Sat}	800 bar	1000 bar	2000 bar	5000 bar
$Y^{3+} + Cl^- = YCl^{2+}$						$Y^{3+} + 2 Cl^- = YCl_2^+$				
25	0.65	1.04	1.13	1.51	2.26	-8.31	-9.14	-9.33	-10.14	-11.74
50	0.22	0.48	0.54	0.81	1.36	-6.58	-7.34	-7.51	-8.27	-9.86
100	0.02	0.13	0.16	0.27	0.51	-3.38	-4.14	-4.30	-5.03	-6.61
150	0.43	0.43	0.43	0.44	0.45	-0.50	-1.37	-1.55	-2.33	-3.96
200	1.24	1.12	1.09	0.99	0.80	2.21*	1.12	0.90	0.01	-1.76
250	2.37*	2.06	2.00	1.78	1.37	4.96*	3.46	3.18	2.09	0.12
300	3.87*	3.21	3.10	2.71	2.07	8.11	5.78	5.40	4.02	1.76
350	6.21*	4.58	4.39	3.75	2.84	12.90	8.24	7.68	5.87	3.24
400		6.26	5.90	4.89	3.64		11.05	10.15	7.68	4.60
450		8.39	7.69	6.13	4.48		14.48	12.94	9.49	5.86
500		11.14	9.85	7.45	5.33		18.77	16.16	11.32	7.05
$Y^{3+} + 3 Cl^- = YCl_3(aq)$						$Y^{3+} + 4 Cl^- = YCl_4^+$				
25	-12.91	-14.00	-14.24	-15.30	-17.38	-14.80	-15.94	-16.19	-17.31	-19.50
50	-10.49	-11.48	-11.71	-12.69	-14.77	-12.16	-13.20	-13.43	-14.47	-16.66
100	-6.07	-7.06	-7.27	-8.22	-10.28	-7.35	-8.39	-8.62	-9.62	-11.78
150	-2.12	-3.25	-3.49	-4.50	-6.62	-3.09	-4.27	-4.52	-5.59	-7.82
200	1.56	0.14	-0.14	-1.30	-3.60	0.88	-0.61	-0.91	-2.14	-4.55
250	5.27*	3.32	2.95	1.54	-1.03	4.85	2.79	2.41	0.93	-1.78
300	9.49	6.45	5.95	4.16	1.22	9.35	6.15	5.62	3.74	0.65
350	15.82	9.74	9.01	6.65	3.23	16.06	9.67	8.89	6.41	2.81
400		13.47	12.30	9.08	5.07		13.63	12.40	9.01	4.79
450		18.01	16.00	11.50	6.77		18.45	16.33	11.60	6.62
500		23.65	20.25	13.94	8.38		24.41	20.84	14.20	8.35

Figure 1. Snapshots of Y(III)-Cl complexes at different T, P from MD simulations. (a-d) are configurations obtained from simulations of box 1 under condition of 25 °C 1 bar; 200 °C, 800 bar; 350 °C, 800 bar; 500 °C, 1000 bar, respectively; (f) is the configuration derived at 500 °C and 1000 bar in box 3.

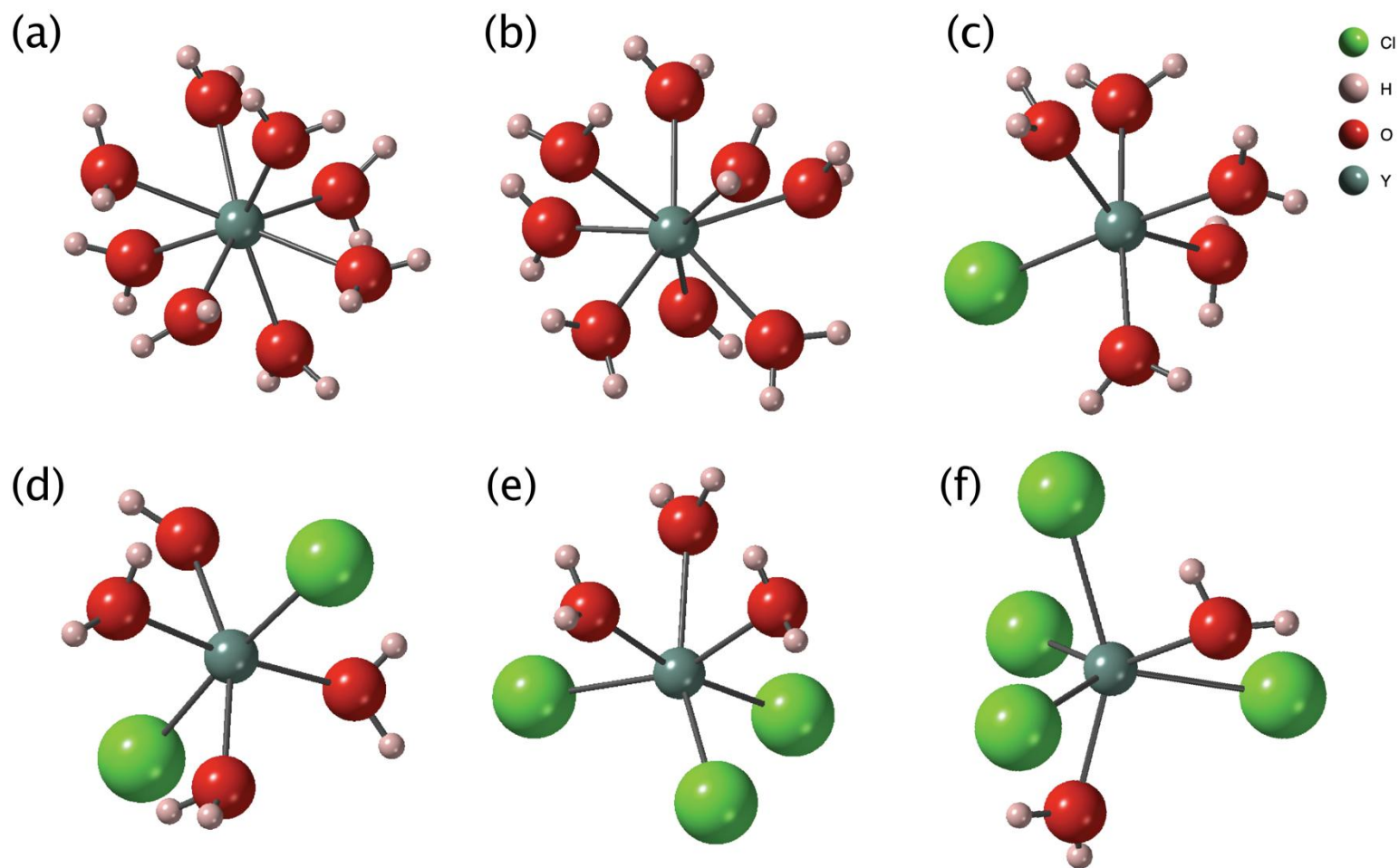


Figure 2, Radial distribution functions (RDF, left axes, solid lines) and their integrals (coordination number, CN, right axes, dash lines) of Y(III)-Cl and Y(III)-O (x-axis) in the four boxes of simulations, (a), (b), box 1; (c),(d), box 2; (e), (f), box 3; (g), (h), box 4.

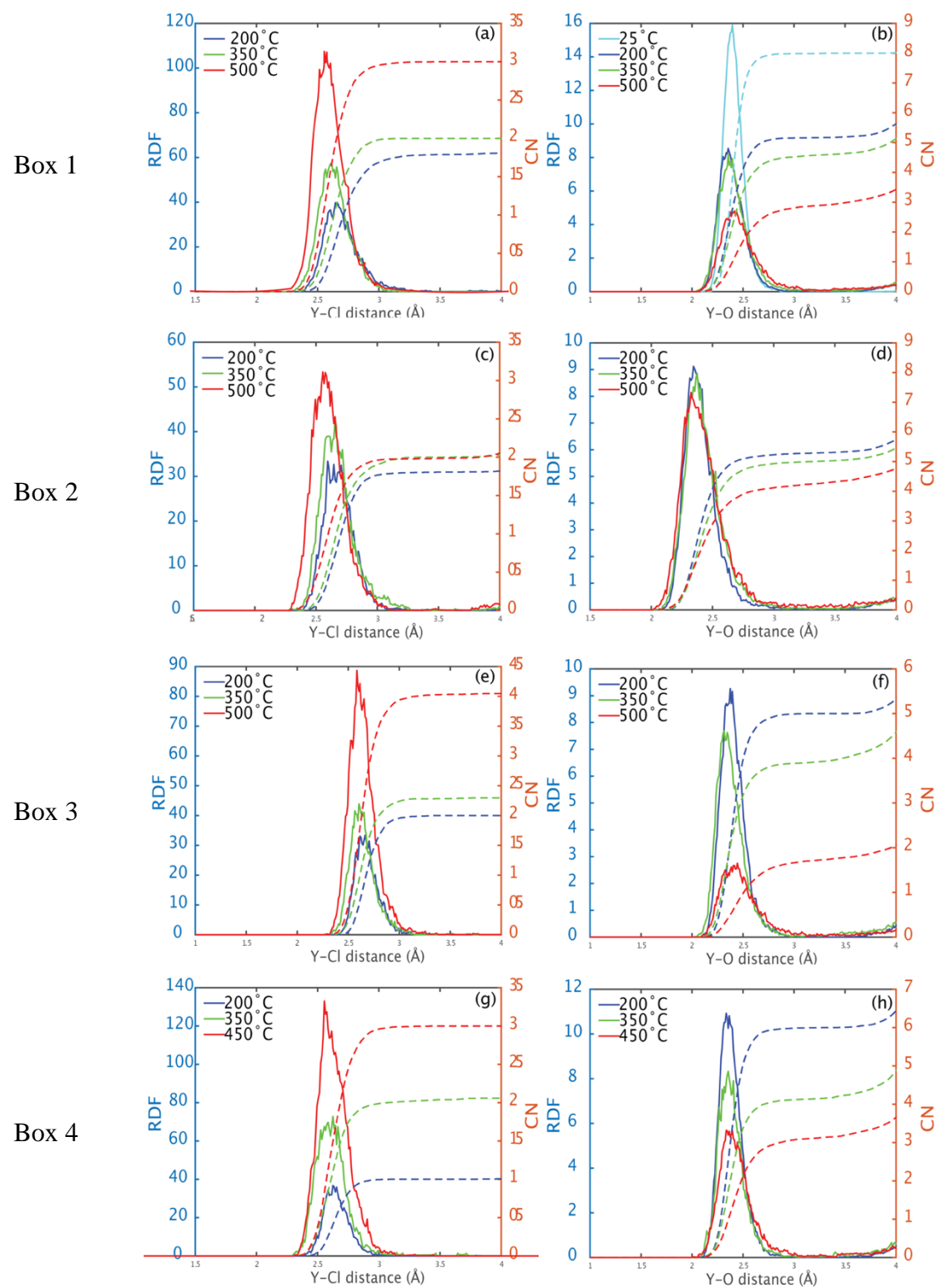


Figure 3. Y(III)-Cl distances over simulation time of (a), job 1a(2) and (b), 1b.

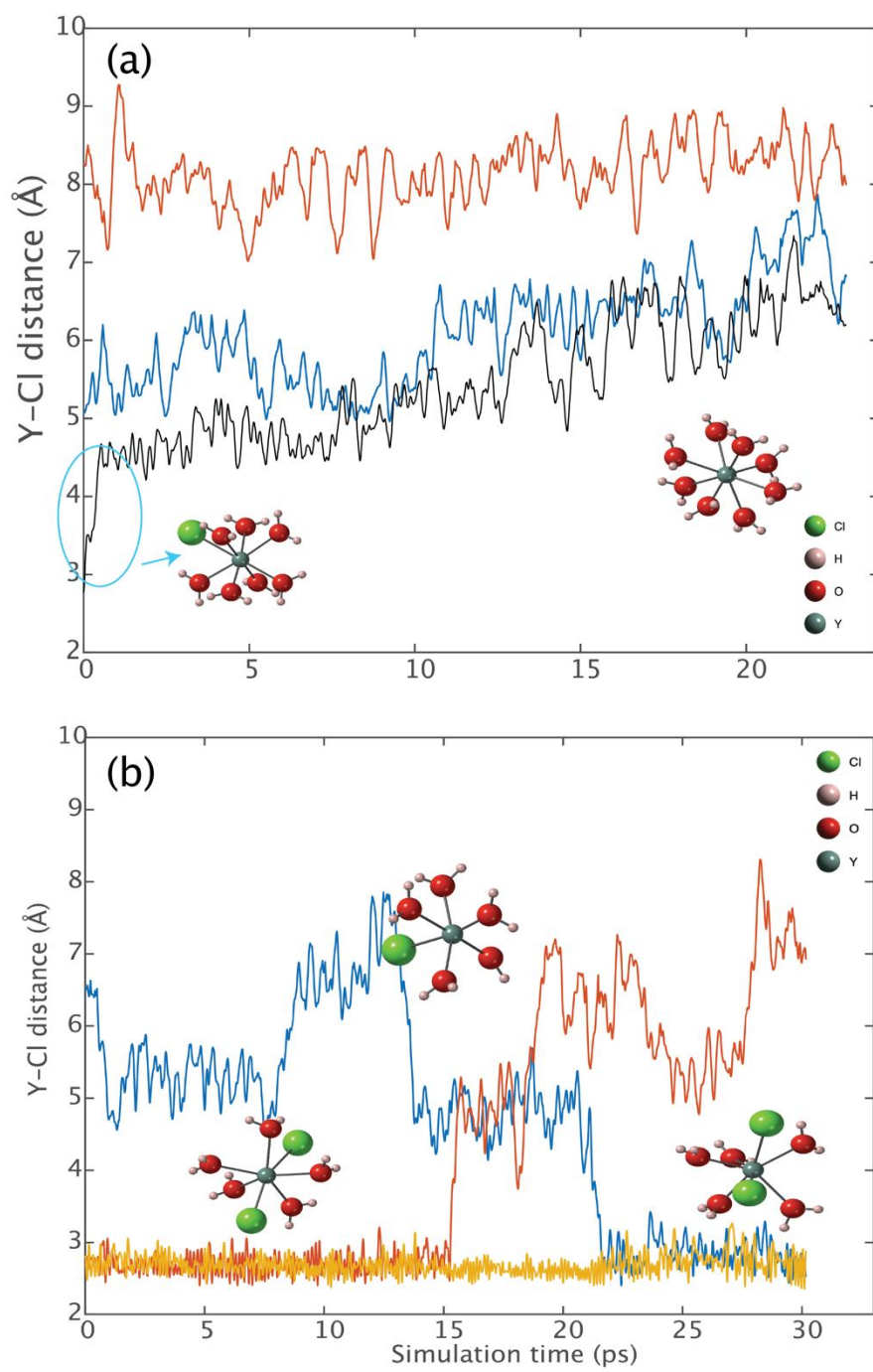


Figure 4. XANES spectra on the solution with highest chlorine concentration (Sol5; 10 m LiCl) as a function of temperature.

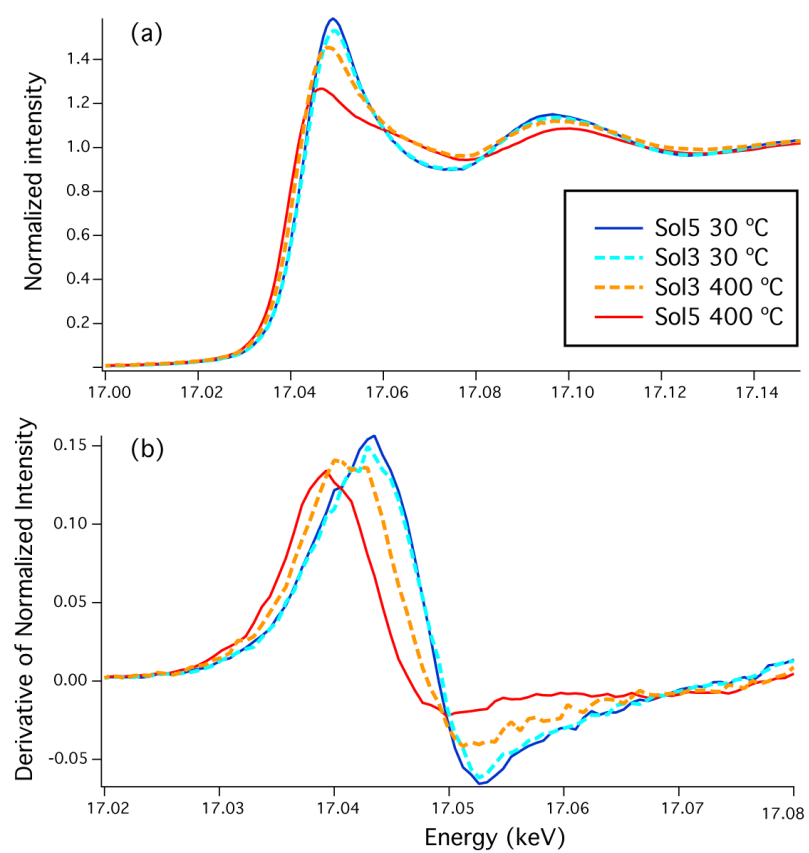


Figure 5. EXAFS data (solid lines) and shell-by-shell fits (dotted lines).

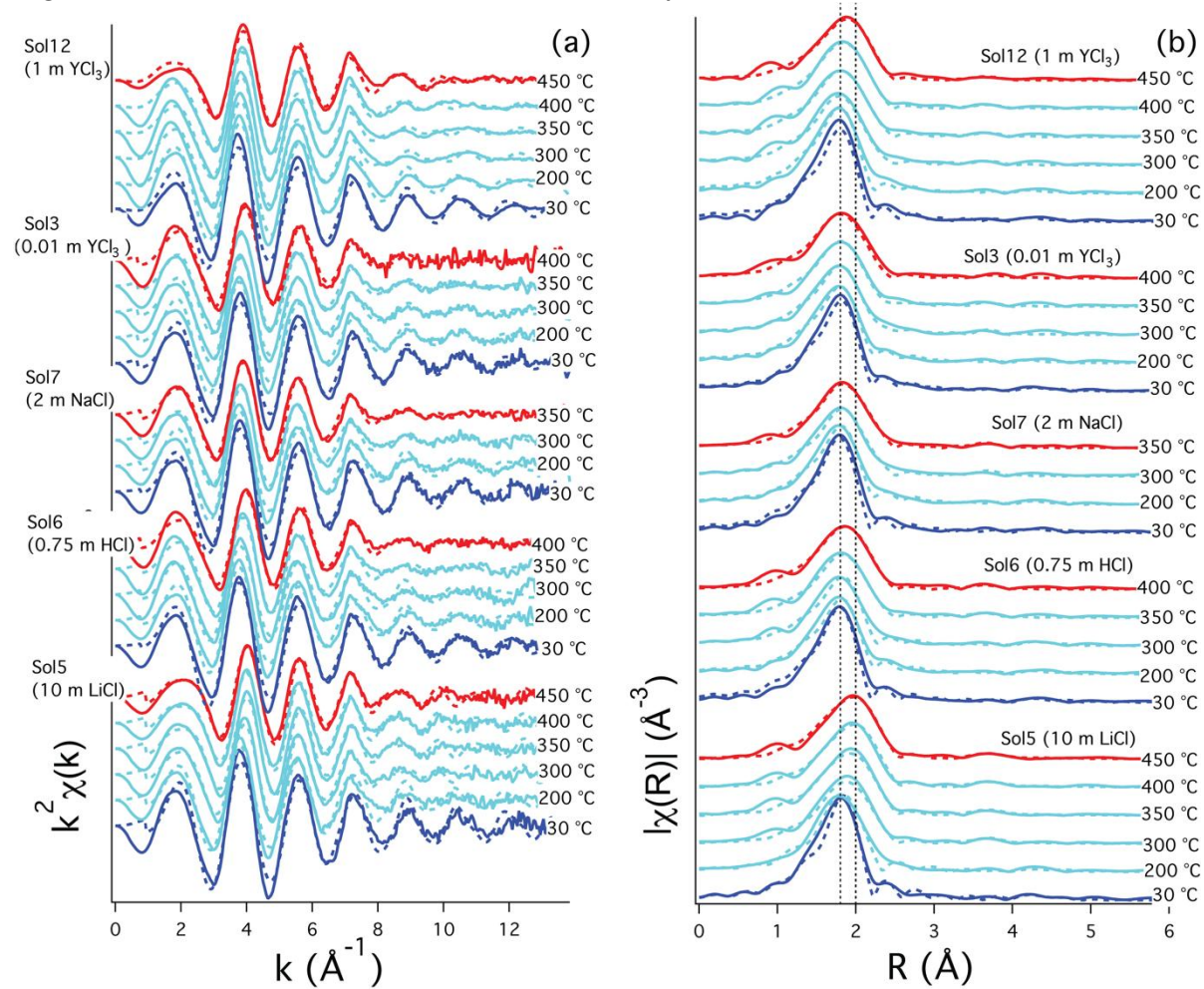


Figure 6. Experimental and calculated XANES spectra: The Yttrium K-edge (17,038 eV) was subtracted from the experimental energy to compared with the FDMNES spectra. (a) crystalline $\text{Y}_2\text{O}_3(\text{s})$; the crystal structure used for FDMNES is from Santos et al. (2005); (b) antiprism $[\text{YO}_8]$ moiety with different bond distance (r) and angle between Y-O bond and z axis (angle θ); (c) triangular prismatic $[\text{YCl}_n\text{O}_{6-n}]$ ($n \leq 3$) moiety with bond distances $r_{\text{Y-O}} = 2.37 \text{ \AA}$ and $r_{\text{Y-Cl}} = 2.65 \text{ \AA}$, compared to selected Y-O-Cl complexes from the MD simulations; and (d) the average of calculated spectra from MD boxes compared to experimental spectra over a range of conditions.

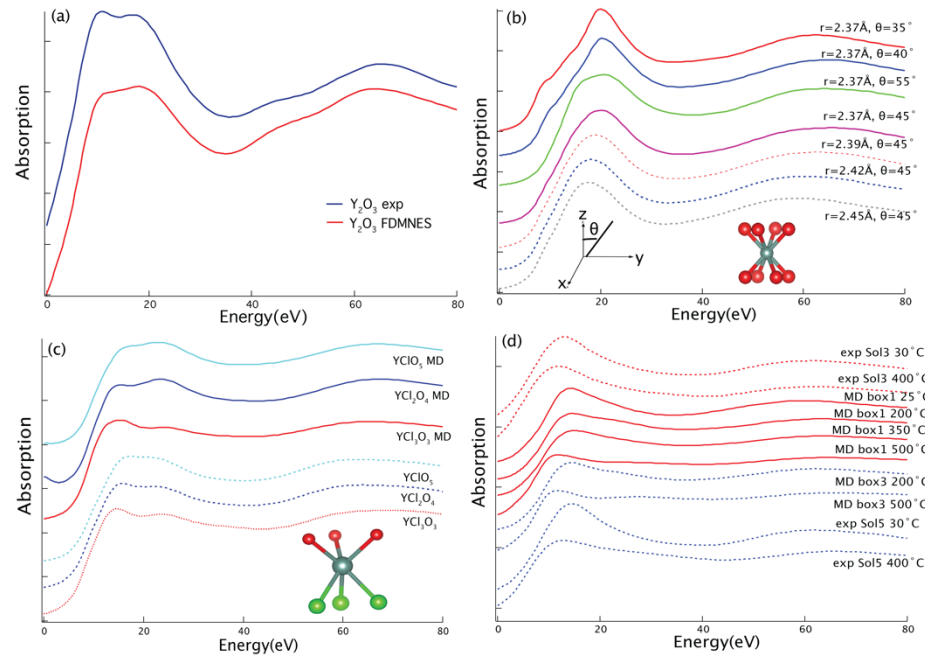


Figure 7. Constraint mean force and free energy surface of dissociation reaction of YCl^{2+} at 200 °C, 800 bar.

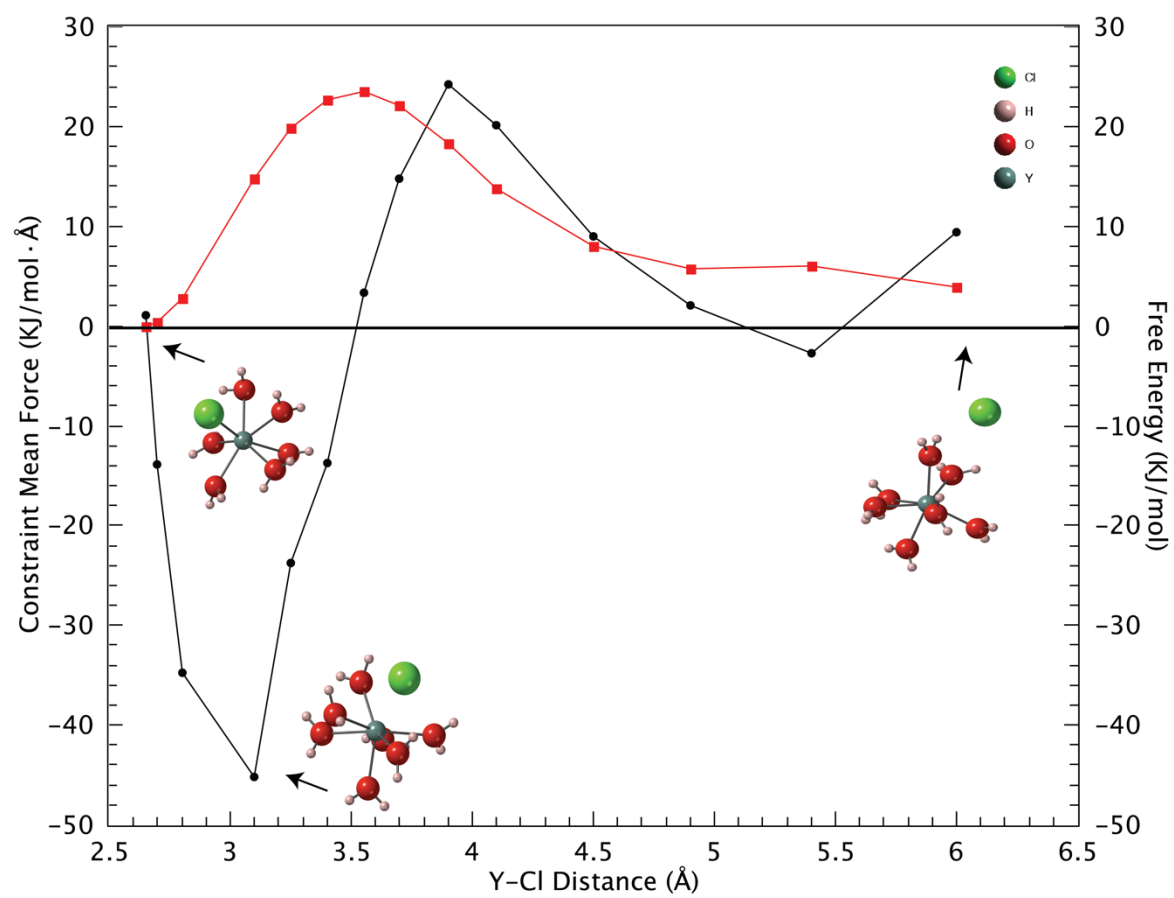


Figure 8. Free energy surface of Y(III)-Cl complexes at 200 °C, 800 bar; 350 °C, 800 bar; 500 °C, 1000 bar from thermodynamic integration calculation in box 1 (a - c) and box 3(d - f).

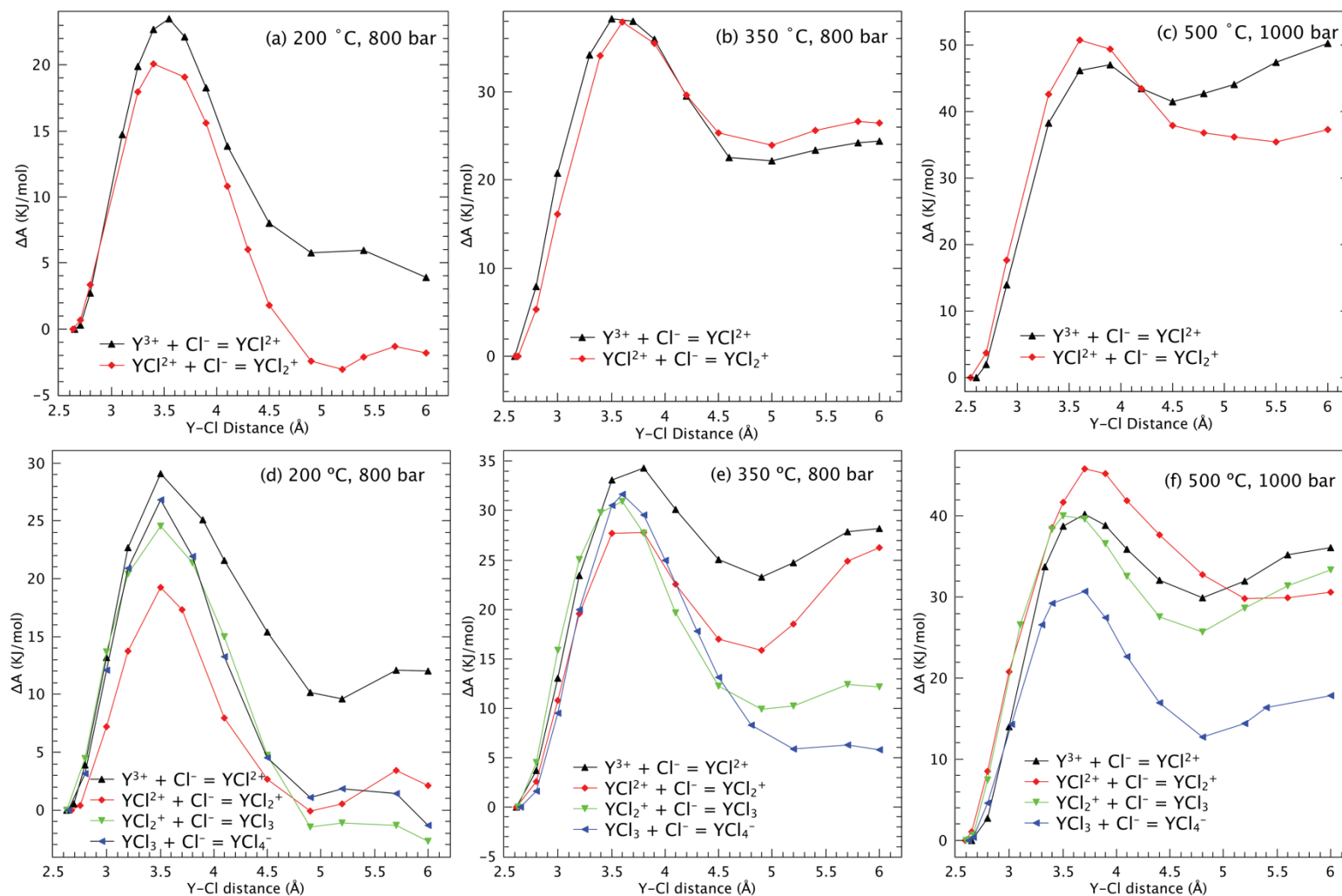


Figure 9. The stepwise $\log K^\ominus$ of association of Y(III)-Cl complexes at 200 °C, 800 bar; 350 °C, 800 bar; 500 °C, 1000 bar and within error bar, and the average value of the two boxes.

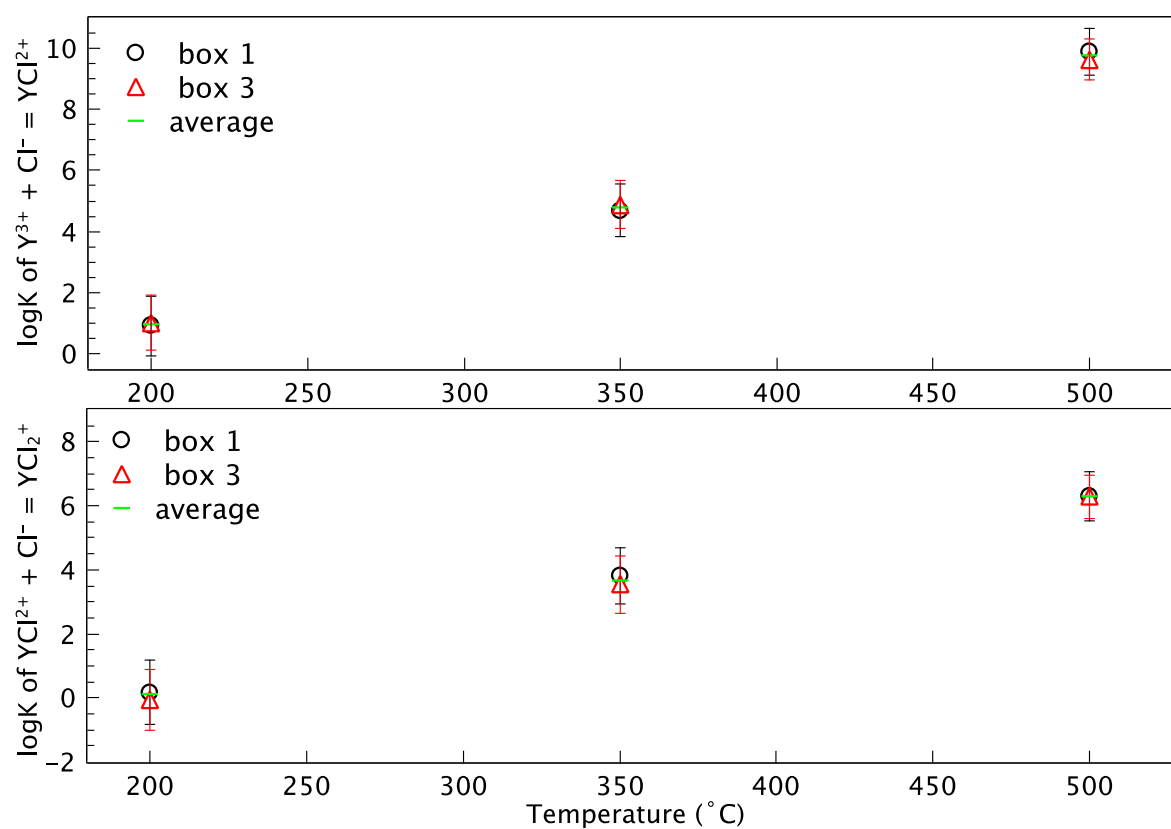


Figure 1 consists of three panels (a, b, c) showing the coordination number (CN) as a function of temperature (°C) for different samples and conditions. The y-axis represents the Coordination Number (CN) from 0 to 10, and the x-axis represents Temperature (°C) from 0 to 500.

(a) $Cl_{tot} = 3$ m

- XAS Sol 12 (blue lines):**
 - CN_{total} (dashed line): Starts at ~8.0 at 0°C, remains relatively constant until ~200°C, then decreases to ~7.2 at 450°C.
 - CN_O (solid line): Starts at ~8.0 at 0°C, decreases steadily to ~3.0 at 500°C.
 - CN_{Cl} (solid line): Starts at ~0.5 at 200°C, increases to ~3.0 at 500°C.
- MD box 1 (red lines):**
 - CN_{total} (dashed line): Starts at ~8.0 at 0°C, decreases to ~6.0 at 500°C.
 - CN_O (solid line): Starts at ~8.0 at 0°C, decreases to ~3.0 at 500°C.
 - CN_{Cl} (solid line): Starts at ~1.8 at 200°C, increases to ~3.0 at 500°C.

(b) $Cl_{tot} = 10$ m(XAS)/5 m(MD)

- XAS Sol 5 (blue lines):**
 - CN_{total} (dashed line): Starts at ~7.5 at 0°C, decreases to ~6.0 at 300°C, then remains constant until 500°C.
 - CN_O (solid line): Starts at ~7.5 at 0°C, decreases to ~3.0 at 400°C, then increases to ~3.0 at 500°C.
 - CN_{Cl} (solid line): Starts at ~1.0 at 200°C, increases to ~3.0 at 500°C.
- MD box 3 (red lines):**
 - CN_{total} (dashed line): Starts at ~7.5 at 0°C, decreases to ~6.0 at 300°C, then remains constant until 500°C.
 - CN_O (solid line): Starts at ~5.0 at 200°C, decreases to ~3.0 at 400°C, then increases to ~4.0 at 500°C.
 - CN_{Cl} (solid line): Starts at ~2.0 at 200°C, increases to ~3.0 at 500°C.

(c) $Cl_{tot} = 2.5$ m

- XAS Sol 7 (blue lines):**
 - CN_{total} (dashed line): Starts at ~8.0 at 0°C, decreases to ~7.2 at 350°C, then remains constant until 500°C.
 - CN_O (solid line): Starts at ~8.0 at 0°C, decreases to ~5.0 at 350°C, then increases to ~3.0 at 500°C.
 - CN_{Cl} (solid line): Starts at ~0.0 at 200°C, increases to ~3.0 at 500°C.
- MD box 4 (red lines):**
 - CN_{total} (dashed line): Starts at ~8.0 at 0°C, decreases to ~6.0 at 350°C, then remains constant until 500°C.
 - CN_O (solid line): Starts at ~6.0 at 200°C, decreases to ~4.0 at 350°C, then increases to ~3.0 at 500°C.
 - CN_{Cl} (solid line): Starts at ~1.0 at 200°C, increases to ~3.0 at 500°C.

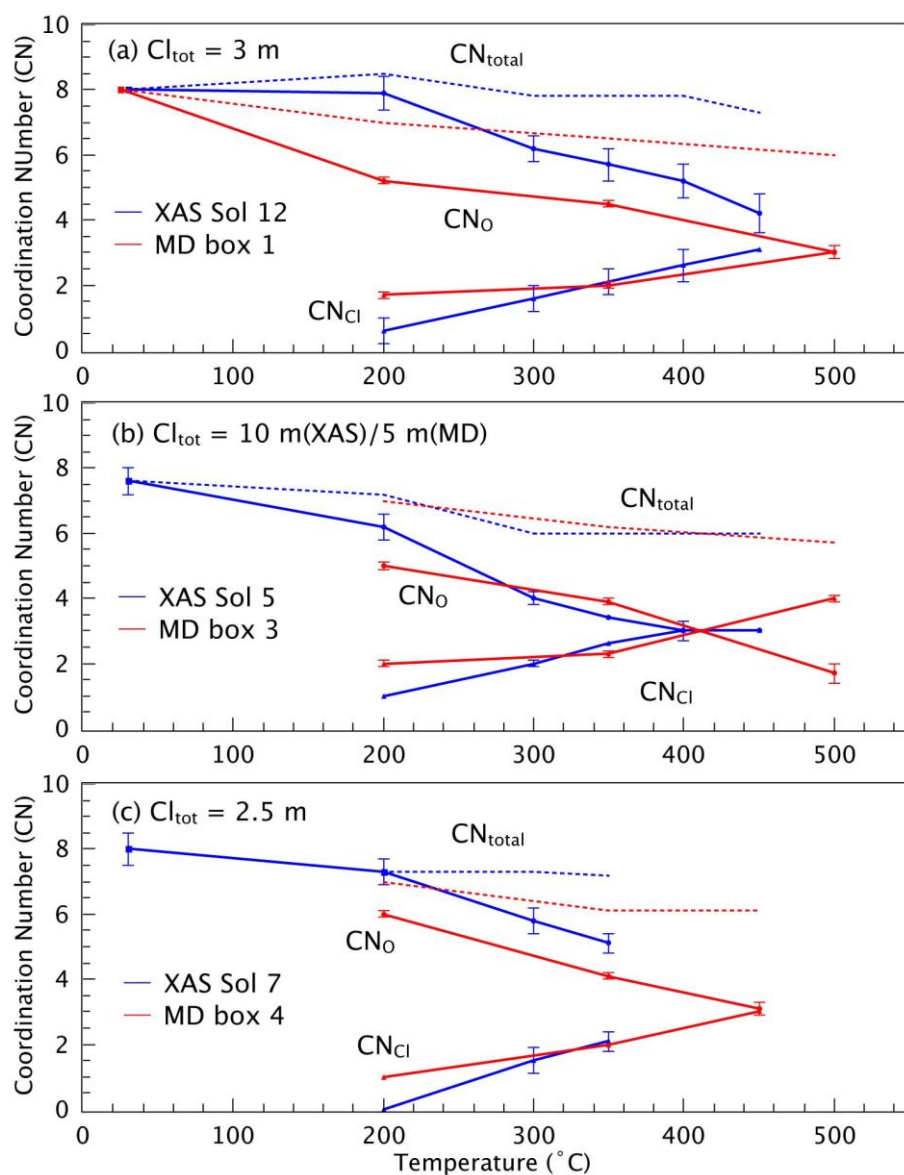


Figure 11. The distribution of Y(III) chloride species at 200 °C, 800 bar; 350 °C, 800 bar; 500 °C, 1000 bar, and pH =3 and 0.3. The solution starts with 0.01 m of Y^{3+} and 0.03 m Cl^- . Dashed lines are average coordination numbers (right axis) from the modelled distribution of species, orange dots are average coordination numbers from XAS Sol 3 at $n(Cl^-) = 0.003$ m (a); Sol 7 at $n(Cl^-) = 2.5$ m and (b,c) Sol 5 at $n(Cl^-) = 5$ m (b,d,f). Errors bars corresponding to ± 0.2 Cl^- ions were added for XAS solutions where this number was fixed, based on fits using different fixed numbers.

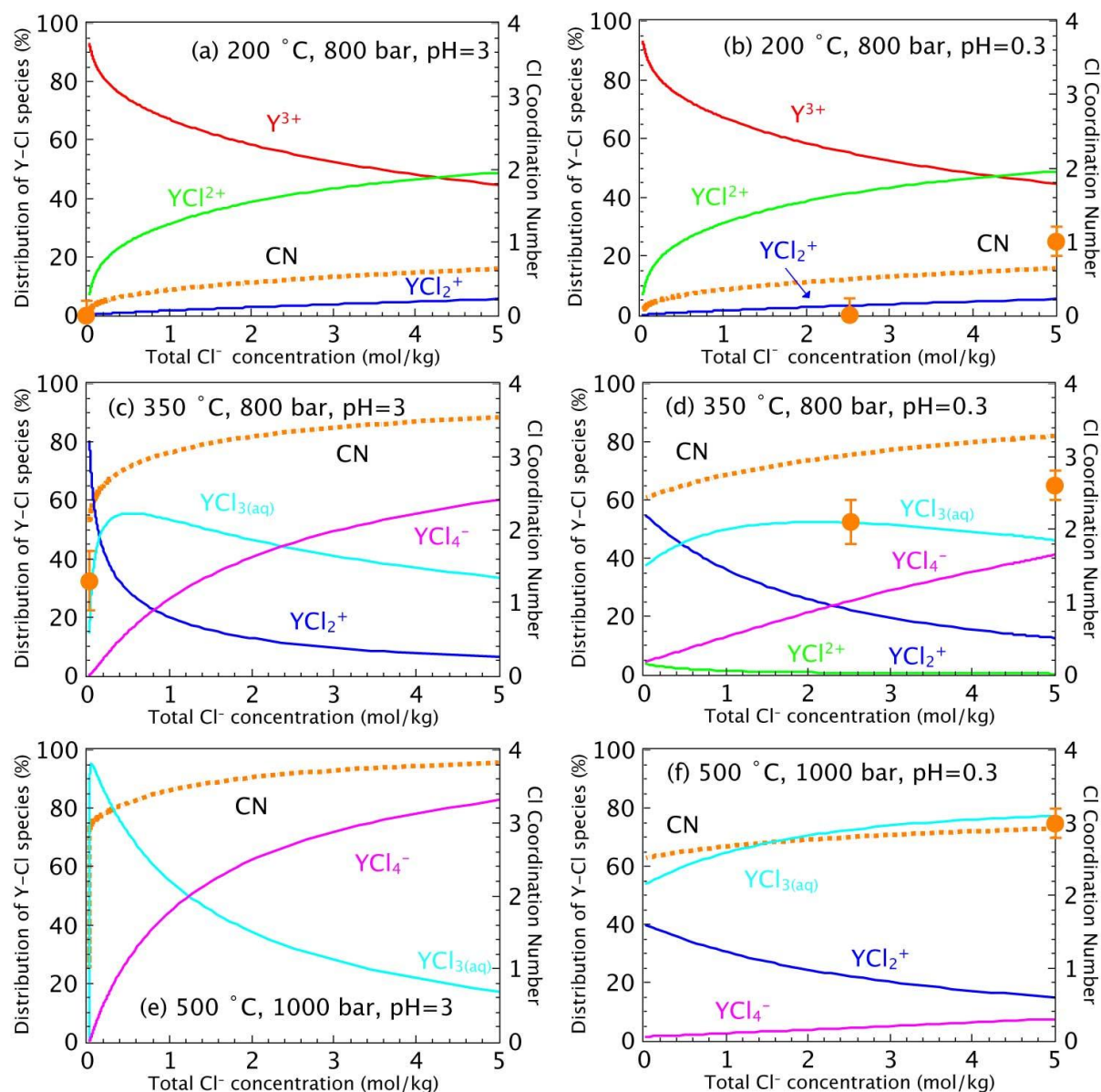


Figure 12. Comparison of the formation constants of REECl^{2+} and REECl_2^+ , measured from solubility experiment from Migdisov (2009); ∇ , predicted from HKF parameters from Migdisov (2016); \times , predicted from MRB model in this study.

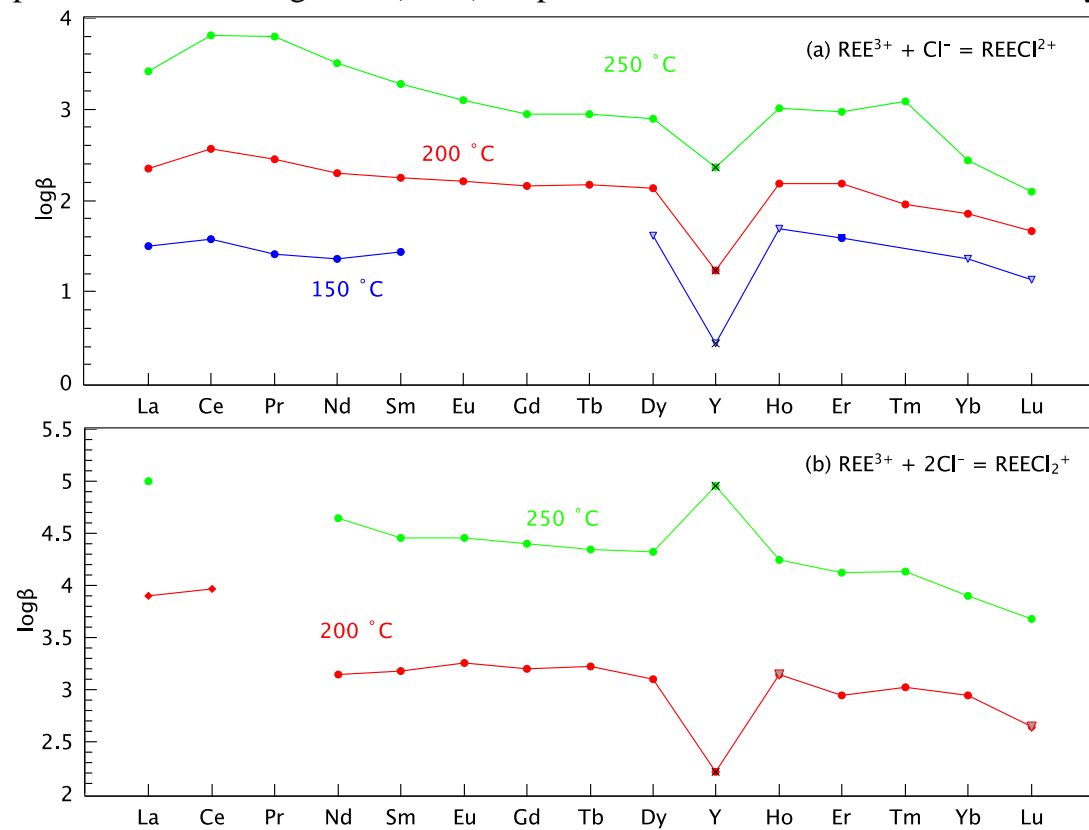


Figure 13. Ho-Cl/Y-Cl species with Cl concentration at 250 °C P_{sat} . The solution starts with 0.001 m Y/Ho and 0.003 m Cl^- , pH=4.

